



LJMU Research Online

Aouad, CJ, Mazzali, PA, Ashall, C, Tanaka, M and Hachinger, S

Abundance stratification in type Ia supernovae – VII. The peculiar, C-rich iPTF16abc: highlighting diversity among luminous events

<http://researchonline.ljmu.ac.uk/id/eprint/24233/>

Article

Citation (please note it is advisable to refer to the publisher's version if you intend to cite from this work)

**Aouad, CJ, Mazzali, PA, Ashall, C, Tanaka, M and Hachinger, S (2024)
Abundance stratification in type Ia supernovae – VII. The peculiar, C-rich iPTF16abc: highlighting diversity among luminous events. *Monthly Notices of the Royal Astronomical Society*. 529 (4). pp. 3838-3857. ISSN 0035-8711**




LJMU has developed **LJMU Research Online** for users to access the research output of the University more effectively. Copyright © and Moral Rights for the papers on this site are retained by the individual authors and/or other copyright owners. Users may download and/or print one copy of any article(s) in LJMU Research Online to facilitate their private study or for non-commercial research. You may not engage in further distribution of the material or use it for any profit-making activities or any commercial gain.

The version presented here may differ from the published version or from the version of the record. Please see the repository URL above for details on accessing the published version and note that access may require a subscription.

For more information please contact researchonline@ljmu.ac.uk

<http://researchonline.ljmu.ac.uk/>

Abundance stratification in type Ia supernovae – VII. The peculiar, C-rich iPTF16abc: highlighting diversity among luminous events

Charles J. Aouad ¹★, Paolo A. Mazzali,^{1,2} Chris Ashall ³, Masaomi Tanaka ^{4,5} and Stephan Hachinger⁶

¹*Astrophysics Research Institute, Liverpool John Moores University, 146 Brownlow Hill, Liverpool L3 5RF, UK*

²*Max-Planck Institut für Astrophysik, Karl-Schwarzschild-Str. 1, D-85748 Garching, Germany*

³*Department of Physics, Virginia Tech, 850 West Campus Drive, Blacksburg, VA 24061, USA*

⁴*Astronomical Institute, Tohoku University, Aoba, Sendai 980-8578, Japan*

⁵*Division for the Establishment of Frontier Sciences, Organization for Advanced Studies, Tohoku University, Sendai 980-8577, Japan*

⁶*Leibniz Supercomputing Centre (LRZ) of the BAdW, Boltzmannstr. 1, D-85748 Garching, Germany*

Accepted 2024 March 12. Received 2024 March 8; in original form 2024 February 8

ABSTRACT

Observations of Type Ia supernovae (SNe Ia) reveal diversity, even within assumed subcategories. Here, the composition of the peculiar iPTF16abc (SN 2016bln) is derived by modelling a time series of optical spectra. iPTF16abc’s early spectra combine traits of SNe 1999aa and 1991T known for weak Si II λ 6355 and prominent Fe III features. However, it differs with weak early Fe III lines, and persistent C II lines post-peak. It also exhibits a weak Ca II H&K feature aligning it with SN 1991T, an observation supported by their bolometric light curves. The early attenuation of Fe III results from abundance effect. The weakening of the Si II λ 6355 line, stems from silicon depletion in the outer shells, a characteristic shared by both SNe 1999aa and 1991T, indicating a common explosion mechanism that terminates nuclear burning at around $12\,000\text{ km s}^{-1}$ unseen in normal events. Beneath a thin layer of intermediate mass elements (IMEs) with a total mass of 0.18 M_{\odot} , extends a ^{56}Ni rich shell totaling 0.76 M_{\odot} and generating a bolometric luminosity as high as $L_{\text{peak}} = 1.60 \pm 0.1 \times 10^{43}\text{ ergs s}^{-1}$. Inner layers, typical of SNe Ia, hold neutron-rich elements, (^{54}Fe and ^{58}Ni), totaling 0.20 M_{\odot} . Stable iron, exceeding solar abundance, and carbon, coexist in the outermost layers, challenging existing explosion models. The presence of carbon down to $v \approx 9000\text{ km s}^{-1}$, totalling $\sim 0.01\text{ M}_{\odot}$ unprecedented in this class, links iPTF16abc to SN 2003fg-like events. The retention of 91T-like traits in iPTF16abc underscores its importance in understanding the diversity of SNe Ia.

Key words: line: identification – nuclear reactions, nucleosynthesis, abundances – radiative transfer – supernovae: general – supernovae: individual: iPTF16abc.

1 INTRODUCTION

It is generally accepted that Supernovae type Ia (SNe Ia) result from the thermonuclear disruption of a carbon–oxygen (CO) white dwarf (WD) in a binary orbit (Hillebrandt & Niemeyer 2000; Mazzali et al. 2007; Livio & Mazzali 2018). The width–luminosity relation (WLR; Phillips 1993), linking the peak brightness of their light curves to their width, has established them as standardizable candles, unveiling the accelerated expansion of the Universe (Phillips 1993; Perlmutter et al. 1998; Riess et al. 1998).

The event is thought to initiate when the central temperature reaches $\sim 10^9\text{ K}$ leading to explosive carbon burning. This ignition can occur through accretion from a non-degenerate companion, [single-degenerate scenario (SD); Whelan & Iben (1973)], or by the violent merger of two WDs [double degenerate scenario (DD) Iben & Tutukov (1984)]. In some cases, SNe Ia may also originate from a triple system [Kushnir et al. (2013); for a review see Livio & Mazzali (2018)]. The mass can either attain the Chandrasekhar limit, alternatively, it may exceed it in what is known as a super-

Chandrasekhar mass scenario, or it may eventually fall below it in a sub-Chandrasekhar mass scenario. In all cases, a burning front propagates, unbinds the WD and causes the production of heavy elements including radioactive ^{56}Ni . The decay of ^{56}Ni through the $^{56}\text{Ni} \rightarrow ^{56}\text{Co} \rightarrow ^{56}\text{Fe}$ chain (Pankey 1962; Colgate & McKee 1969) releases γ -rays and positrons, which deposit energy in the expanding ejecta, giving rise to optical photons. These photons remain trapped until they diffuse as the ejecta expand and the opacity decreases. ^{56}Ni and other iron group elements (IGEs) have a rich array of line transitions. Their presence in the H poor ejecta where line opacity dominates (Pauldrach et al. 1996), increases the diffusion time, so events with more ^{56}Ni are not only hotter and brighter, but decline slower leading to the observed Width–Luminosity relation in their light curves (Arnett 1982; Mazzali et al. 2001a; Bersten & Mazzali 2017).

It has been suggested that the observed scatter in their peak luminosity corresponds to different amounts of ^{56}Ni synthesized (a range of $0.1\text{--}1\text{ M}_{\odot}$, Mazzali et al. 2001a, 2008). What causes this spread in ^{56}Ni production is still not clear, but it is a direct consequence of the burning regime. Currently, one of the favored burning scenarios is one in which a deflagration wave (subsonic burning) transits to a detonation wave (supersonic shock wave) in the so-called deflagration to detonation transition model (DDT;

* E-mail: charlesaouad@aacid.ae, C.J.Aouad@2020.ljmu.ac.uk

Khokhlov 1991b; Mazzali et al. 2007). This transition enables efficient burning in the outer layers of the ejecta, resulting in the synthesis of sufficient amounts of intermediate-mass elements (IMEs; e.g. Si, S, Ca) as supported by observations.

A significant proportion of SNe Ia are typically categorized as ‘normal’ owing to the uniformity of their spectroscopic characteristics. Nevertheless, an increasing number of events with a wide array of spectral features have been observed and classified as ‘peculiar’. These peculiar SNe Ia encompass a broad range, from cooler, fainter objects like SN 1991bg (Mazzali et al. 1997), SN 1986G (Ashall et al. 2016), SN 2002cx (Li et al. 2003), SN 2002es (Ganeshalingam et al. 2012) to hotter, more luminous objects such as SN 1991T (Mazzali, Danziger & Turatto 1995) or SN 1999aa (Garavini et al. 2004). Furthermore, within the realm of luminous SNe Ia, there exists a distinct subgroup known as SN 2003fg-like events (Ashall et al. 2021), which are also referred to as super-Chandrasekhar mass events (SC). (e.g. SN 2003fg – Howell et al. 2006, SN 2006gz – Hicken et al. 2007, SN 2009dc – Taubenberger et al. 2011, SN 2012dn – Chakradhari et al. 2014). Yet, despite several attempts to classify their spectra (e.g. Nugent et al. 1995; Benetti et al. 2005; Branch et al. 2006; Wang et al. 2009), a consensus regarding this observed diversity remains elusive.

During the initial stages of a SNe Ia event observed in the optical, known as the photospheric phase, the spectra probe the outer layers. They are characterized by broad P-Cygni profiles indicating expansion velocities of the order of $10\,000\text{ km s}^{-1}$. At this early stage, the main spectral features of the SNe classified as ‘normal’ are lines of singly ionized IMEs such as Si II, S II, Ca II, Mg II, and neutral elements such as O I. As time progresses, deeper layers of the ejecta are revealed and blends of Fe III and Fe II start to influence the appearance of the spectra. (Filippenko 1997; Parrent, Friesen & Parthasarathy 2014).

A few months after reaching maximum light, the ejecta of SNe Ia generally become gradually transparent to gamma-rays, allowing only a fraction of the radioactive energy decay to be deposited (Ashall et al. 2021). Around one year after the explosion, SNe Ia spectra probe the innermost shells of the ejecta and the supernova reaches the so-called nebular phase, whose spectra are characterized by emission, mostly in forbidden [Fe III] and [Fe II] lines (Mazzali et al. 2015).

In contrast to normal Type Ia SNe, the early spectra of the events classified as 1991T-like display distinct behaviour. Singly ionized IMEs like Si II λ 6355, S II, Ca II H&K, and Ca II NIR are either absent or notably weak, while prominent Fe III lines dominate. As the events progress, their spectra gradually transition to resemble those of normal SNe Ia around peak brightness. While most 1991T-like events belong to the shallow silicone (SS) subclass according to the classification scheme of Branch et al. (2006) or to the low velocity gradient (LVG) subclass according to Benetti et al. (2005), substantial diversity exists within this group. For example, the initial spectra of SN 1999aa exhibit Ca II HK and Si II λ 6355 lines with strengths intermediate between those seen in ‘normal’ events and those classified as 91T-like, morphing to resemble the normal events earlier than SN 1991T (Garavini et al. 2004; Aouad et al. 2022). Conversely, the early spectra of the events classified as 2003fg-like showcase numerous deep, singly ionized IME lines, despite many exhibiting high luminosities. They are also characterized by slow photospheric velocities and relatively weak Fe III lines. Additionally, they all exhibit strong and persistent carbon features, the signature of unburnt material in the ejecta, observable until post-maximum epochs.

This spectral diversity challenges our understanding of these objects and their reliability as precise distance indicators. This is especially important for the bright events, which are of particular

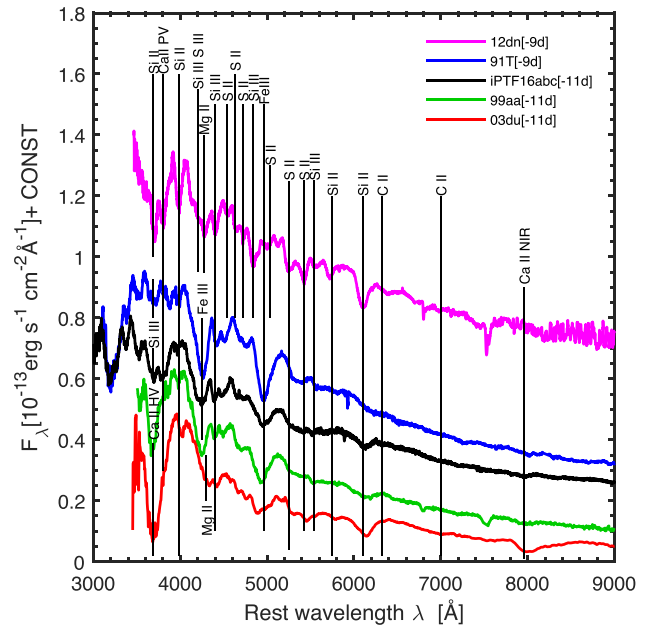


Figure 1. Early time spectra of iPTF16abc in comparison with SN 1991T, SN 1999aa, the normal SN 2003du, and the 03-fg like SN 2012dn. Epochs are shown with reference to B maximum.

significance in cosmology. Therefore, it is important to identify objects whose spectroscopic features link between two or several different spectroscopic classes. iPTF16abc is an example of such an object. It is characterized by early spectra resembling SN 1999aa, however, it shows differences when compared to both SN 1991T and SN 1999aa (cf. Fig. 1). In particular, the Ca II H&K high velocity (HV) feature is of intermediate strength between SN 1999aa and SN 1991T, Fe lines are weaker, and it exhibits a C II $\lambda\lambda$ 6578, 6583 line that slowly fades one week before B maximum, but then reappears one week post maximum. As we progress to one week past peak brightness and extend into the nebular phase, the spectra of these three events become nearly indistinguishable (cf. Figs 2 and 3). Remarkably, such properties are not completely different from those observed in 2003fg-like events. All this establishes iPTF16abc as a captivating event, highlighting the subtle spectroscopic diversity that exists within the realm of luminous peculiar events.

In this paper, we employ abundance tomography as a method to investigate SNe Ia, allowing us to map the internal composition of the expanding ejecta and gain insights into the explosion process (Stehle et al. 2005; Mazzali et al. 2008; Tanaka et al. 2011; Sasdelli et al. 2014; Ashall et al. 2016; Aouad et al. 2022). We apply this technique to analyse iPTF16abc and compare it to SN 1999aa, SN 1991T, and the normal SN 2003du. While we draw some parallels with 2003fg-like events, a comprehensive exploration of this aspect is reserved for future investigations. One of the main strengths of our work is that we have been applying a similar modelling technique to analyse and compare different events. This increases confidence that the similarities and differences identified between different SNe Ia are real and not limited by the modelling technique. The paper’s structure is as follows: Sections 2 and 3 discuss data and methods, Sections 4 and 5 present models for photospheric phase spectra, Section 6 focuses on the nebular spectrum model, Section 7 discusses the abundance stratification while Section 8 outlines a light curve model based on our abundance stratification results. Section 9 discusses our findings and Section 10 concludes the paper.

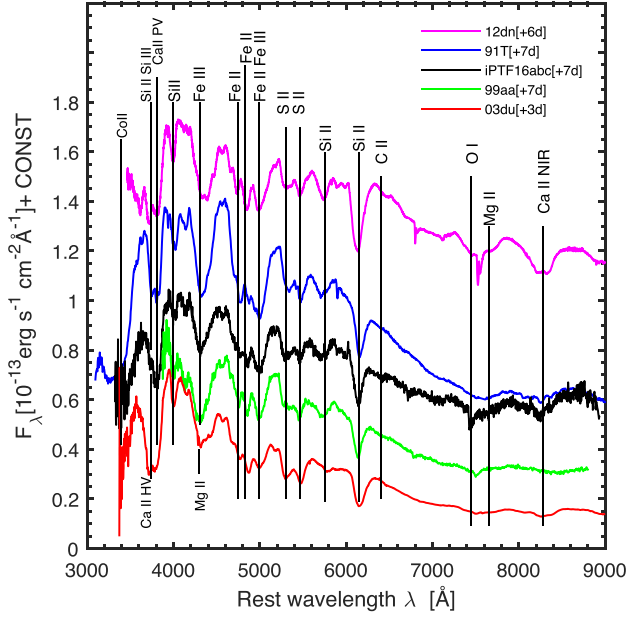


Figure 2. One week post maximum spectrum of iPTF16abc in comparison with SN 1991T, SN 1999aa, the normal SN 2003du, and the 03-fg-like SN 2012dn. Epochs are shown with reference to B maximum.

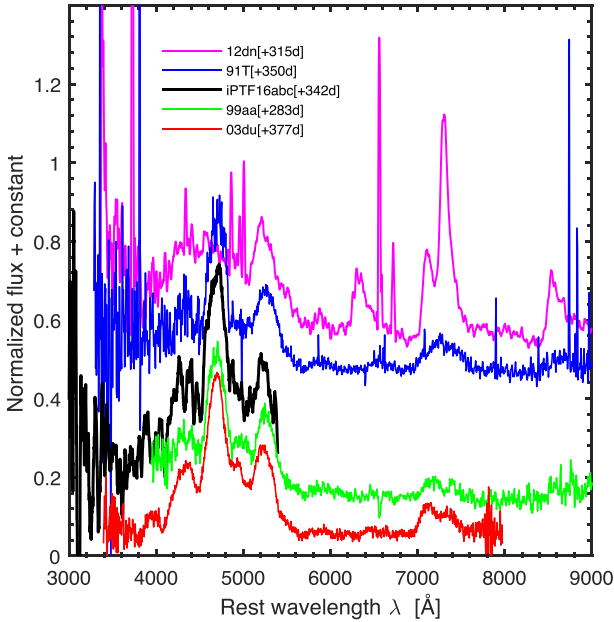


Figure 3. Nebular spectrum of iPTF16abc in comparison with SN 1991T, SN 1999aa, the normal SN 2003du, and the 03-fg-like SN 2012dn. Epochs are shown with reference to B maximum.

2 DATA

iPTF16abc (IAU name: SN 2016bln) was discovered by the intermediate Palomar Transient Factory on 2016, April 4, at 09:21:36.000, JD = 2457482.89 (Gal-Yam 2016), in the tidal tail of NGC 5221, a barred galaxy classified as SABb at a redshift of 0.023279 (Courtois & Tully 2015). Reported distance moduli, μ , to the host galaxy, using

Table 1. Spectra of SN iPTF16abc and modelling parameters.

UT Date 2016	JD ^a	Epoch ^b (days)	Telescope/Instr.	log L [L_{\odot}]	v (km s ⁻¹)	T_{ph} (K)
05/04 ^c	483.3	-15.3	Gemini-N/GMOS	8.860	13 450	15 900
10/04 ^c	488.4	-11.0	Keck-I/LRIS	9.370	12 200	14 670
11/04 ^c	489.5	-9.8	LCO-2m/FLOYDS	9.470	12 000	14 935
12/04 ^c	490.4	-8.9	LCO-2m/FLOYDS	9.550	11 800	14 832
13/04 ^c	491.5	-7.8	LCO-2m/FLOYDS	9.580	11 200	15 330
25/04 ^c	503.3	+3.7	LCO-2m/FLOYDS	9.620	10 000	10 187
28/04 ^c	506.0	+6.3	NOT/ALFOSC	9.610	9 200	10 040
30/04 ^c	508.3	+8.5	LCO-2m/FLOYDS	9.520	7 500	9 682
29/03/2017 ^c	841.7	+342.4	Keck-I/LRIS	-	-	-

Notes. ^a JD - 2457 000

^b Rest-frame time since B maximum

^c see Dhawan et al. (2018)

the Tully–Fisher relation, vary from 34.69 to 35.09¹ (Willick et al. 1997; Karachentsev et al. 2006; Theureau et al. 2007; Makarov et al. 2014). We adopt an extinction value $E(B - V)$ of 0.05 for the Milky Way (Ferretti et al. 2017) and 0.03 for the host galaxy (Schlafly & Finkbeiner 2011; Miller et al. 2018). Early time photometric data in the U , B , V , r , and i bands were taken from Miller et al. (2018) and late-time g band data were taken from Dhawan et al. (2018), who reports a $\Delta m_{15}(B)$ of 0.91. Spectroscopic observations of iPTF16abc in the photospheric phase were obtained with a variety of telescopes and instruments. A nebular spectrum was obtained 342 days after B maximum on 2017-03-29 by Dhawan et al. (2018). The time of the B -band maximum light was considered to be on Modified Julian Date (MJD) 57499.54, as adopted in Miller et al. (2018). Photocalibration was performed in the U , B , V , r , bands by multiplying the spectra with a low-order smoothed spline. The calibrated flux does not deviate by more than 10 per cent from the interpolated photometry data in any pass band. The spectra used in the current study are listed in Table 1.

3 MODELLING TECHNIQUES OF THE PHOTOSPHERIC PHASE

We use a 1D Monte Carlo radiative transfer code as laid out in Mazzali & Lucy (1993), Lucy (1999a, b), Mazzali (2000), Stehle et al. (2005). The code computes the radiative transfer through the expanding ejecta at a given epoch. It assumes a sharply defined spherical photosphere from which a continuous blackbody radiation with temperature T_{ph} is emitted. Seconds after the initial explosion, the ejecta is assumed to coast on a homologous expansion in which the radius is proportional to the velocity i.e. $r = v \times t$, therefore the velocity of the photosphere v_{ph} can be used as a spatial coordinate assuming a time t from the explosion. As the ejecta expand, the photosphere recedes in mass coordinates. Photons emitted at this photosphere propagate through the ejecta and undergo Thomson scattering or intersect with the lines assuming the Sobolev approximation (Sobolev 1960; Castor 1970). Bound–bound emissivity is treated through a branching scheme (Mazzali 2000). Ionization and excitation levels are calculated assuming a nebular approximation (cf. Mazzali 2000). In this approximation, the gas state depends strongly on a radiation temperature T_{R} , computed from the mean frequency of the radiation field at every radial mesh, and a dilution factor which parametrizes the radiation field energy density as a function of radius. The radiation field and the gas state are iterated until T_{R} is converged to the percent level. T_{ph} is automatically adjusted to match the given L_{bol} taking in consideration the back-scattering rate.

¹<http://leda.univ-lyon1.fr/>

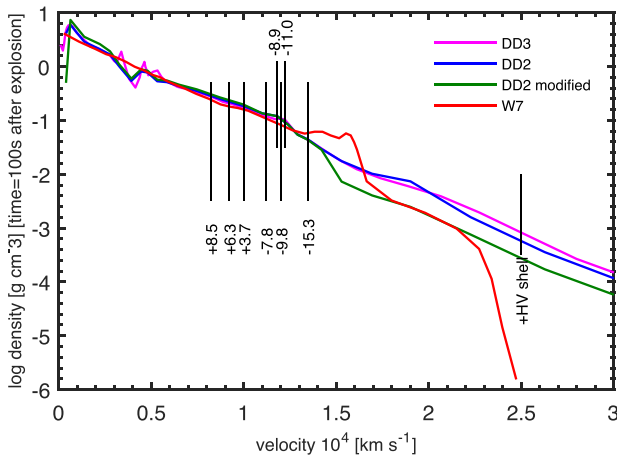


Figure 4. Density profiles used in the modelling process: W7 (Nomoto et al. 1984), DD2, DD3 (Iwamoto et al. 1999), and the modified DD2. In the modified DD2, a mass of $0.05 M_{\odot}$ has been removed at $v > 14\,000 \text{ km s}^{-1}$ and redistributed in the inner layers to conserve the total mass. The total Kinetic energy is not significantly changed due to the small mass shift. Vertical dashed lines mark the photospheres of the synthetic spectra.

The code requires an initial fixed density profile of the SN ejecta, in addition to the input parameters v_{ph} , L_{bol} , t , and the abundances in every shell which are manually optimized to match the observed data. For a detailed description of the modelling procedure see Stehle et al. (2005) and Mazzali et al. (2014), and for a discussion on errors see Ashall & Mazzali (2020).

4 THE PHOTOSPHERIC PHASE

We analysed eight spectra obtained from 15 days before to 8 days after B maximum. To model these spectra, we employed four distinct density profiles, namely one fast-deflagration (W7), two delayed detonation models (DD2 and DD3, Nomoto, Thielemann & Yokoi 1984; Iwamoto et al. 1999) and one modified DD2 density profile (see Section 5); The density profiles are shown in Fig. 4. W7, DD2, and DD3, correspond to well-known hydrodynamic models that have been successfully used to model a number of SNe Ia and reproduce the majority of their observed spectroscopic features, both during the photospheric and the nebular phases as well as their light curves (Stehle et al. 2005; Mazzali et al. 2008; Tanaka et al. 2011; Ashall et al. 2016, 2018; Aouad et al. 2022). Using the same density profiles when modelling different supernovae enables comparison between different events, as is the focus of this series of papers. The input parameters used in the models are shown in Table 1, and the resulting spectra are presented in Figs 5, 6, 7, 14, and 15.

4.1 The pre-maximum spectra

In Figs 5, 6, and 7, we display synthetic spectra from day -15 to day -8 , overlaid on the observed spectra. Our synthetic spectra faithfully replicate the observed features, with a good match in flux across the entire wavelength range. This alignment is evident in Fig. 8, where we compare photometric light curves derived from synthetic spectra with observational measurements. The luminosity exhibits a steep rise from day -15 to day -11 , while the velocities decline slowly to preserve the optimal temperatures required for the synthetic spectra’s ionization equilibrium. Notably, the velocities closely resemble those calculated for SN 1999aa, but they significantly exceed those of

SN 2003du, signaling a substantially higher level of opacity in SN 1999aa and iPTF16abc.

Fe-group elements: The earliest spectrum of iPTF16abc, taken at day -15 , shows Fe III features around 4250 and 5000 \AA that we could reproduce with $X(\text{Fe}) = 0.0035$ at $v > 13\,450 \text{ km s}^{-1}$. This is above solar abundance ($X(\text{Fe}_{\odot}) = 0.001$, Asplund et al. 2009). As we advance to day -11 , these features grow in intensity, corresponding to an increase in the iron mass fraction to 0.025 at $v > 12\,200 \text{ km s}^{-1}$. However, when compared to SNe 1999aa and 1991T at the same epoch (Fig. 1), these features appear comparatively weaker. Consequently, the iron abundance in iPTF16abc remains noticeably lower (Fig. 9). The iron present must be stable (i.e. ^{54}Fe), as it could not have resulted from the decay of ^{56}Ni , at this early stage. Remarkably, the presence of iron at the outermost shell up to $v = 25\,000 \text{ km s}^{-1}$ is not anticipated by any of the explosion models.

These features keep increasing in strength at days -10 and in the following days. Subsequently, the Fe mass fraction gradually increases, reaching a value of 0.038 at day -3.8 at $v > 11\,200 \text{ km s}^{-1}$. At this epoch, this fraction is only ~ 50 per cent of all iron needed, the remaining being the product of ^{56}Ni decay. These stable iron mass fractions values significantly surpass solar abundances, strongly indicating that at these shells ($v < 13\,450 \text{ km s}^{-1}$), iron likely results from explosive nucleosynthesis. These stable iron mass fractions are similar to the ones computed in both the W7 and the DD models (cf. Nomoto et al. 1984; Iwamoto et al. 1999).

A ^{56}Ni mass fraction of 0.013 is required at $v > 13\,450 \text{ km s}^{-1}$, to accurately replicate the Co III $\lambda\lambda 3287, 3305$ feature, observed near 3200 \AA , in spectra taken on day -11 and onwards (cf. Fig. 10). Additionally, this ^{56}Ni mass fraction suppresses the flux in the ultraviolet (UV) range and contributes to redirecting it towards longer wavelengths in the earliest spectrum obtained on day -15 .

Going inwards, the ^{56}Ni mass fraction increases gradually, reaching a peak of 0.69 at $v > 11\,200 \text{ km s}^{-1}$ at day -8 . These values are slightly larger than the ones computed for SNe 1999aa and 1991T at the same epochs. A feature centred around 4700 \AA , primarily influenced by multiple Ni III and S II lines is also replicated in the synthetic spectra. Unfortunately, a comparison with SNe 1999aa and 1991T is not possible at day -15 as data for these events are not available at this early stage.

Calcium: In the majority of SNe Ia, the Ca II H&K feature, seen around 3800 \AA is often composed of two separate components: one at photospheric velocity (PV) and one at high velocity (HV; Mazzali et al. 2005; Childress et al. 2014; Dutta et al. 2021). In the SNe Ia classified as spectroscopically normal, e.g. SN 2003du (Tanaka et al. 2011), the HV component dominates, causing the two features to blend together and form a single deep absorption line. However, the high-velocity component in iPTF16abc at day -11 and after is relatively weak, causing the feature to split into two separate components, with the blue part being of intermediate strength between the one seen in SN 1999aa and the one seen in SN 1991T (cf. Fig. 1). Our synthetic spectra accurately reproduce this behaviour with $X(\text{Ca}) = 0.00055$ at $v > 25\,000 \text{ km s}^{-1}$, which is above Solar abundance ($X(\text{Ca}_{\odot}) = 0.00006$ as reported in Asplund et al. 2009). This fraction decreases to 0.0002 at $v > 13\,450 \text{ km s}^{-1}$ than increases to 0.01 at $v > 12\,200 \text{ km s}^{-1}$ and remains constant until day -9 at $v > 11\,800 \text{ km s}^{-1}$. This calcium mass fraction at lower velocities is necessary to be able to replicate the (PV) component of the feature. Even with this increase in the calcium mass fraction, the prevailing high temperatures maintain the blue component of the feature weak, primarily made by Si III $\lambda\lambda 3796, 3806$ and Co III $\lambda 3782$. This can be seen in Fig. 11, where we generate a synthetic spectrum at day -9 , deliberately excluding any calcium at high

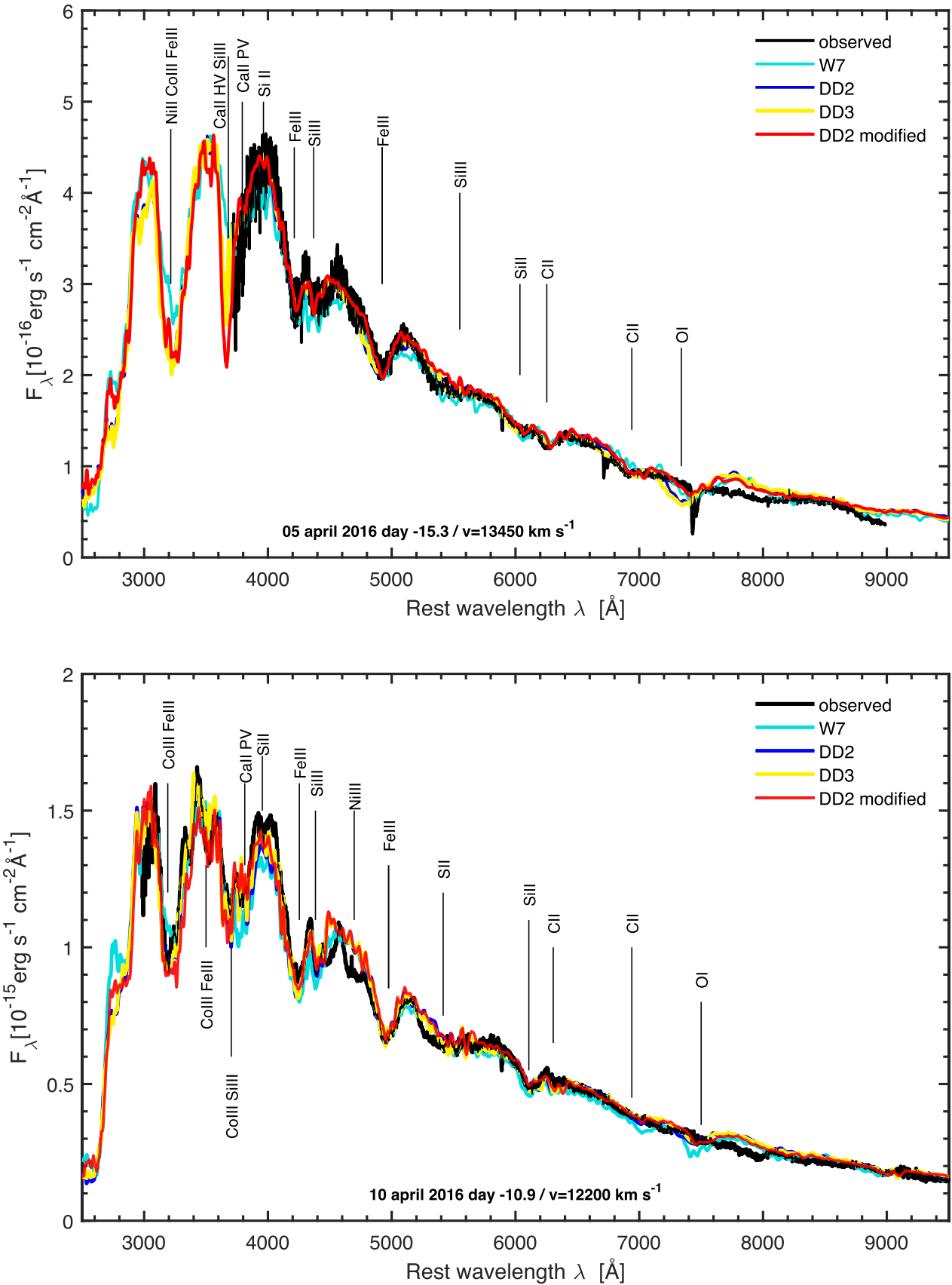


Figure 5. Observed early spectra of iPTF16abc (black), compared to the synthetic spectra in colours, corresponding to different density profiles as indicated in the legend. Epochs are shown with reference to B maximum.

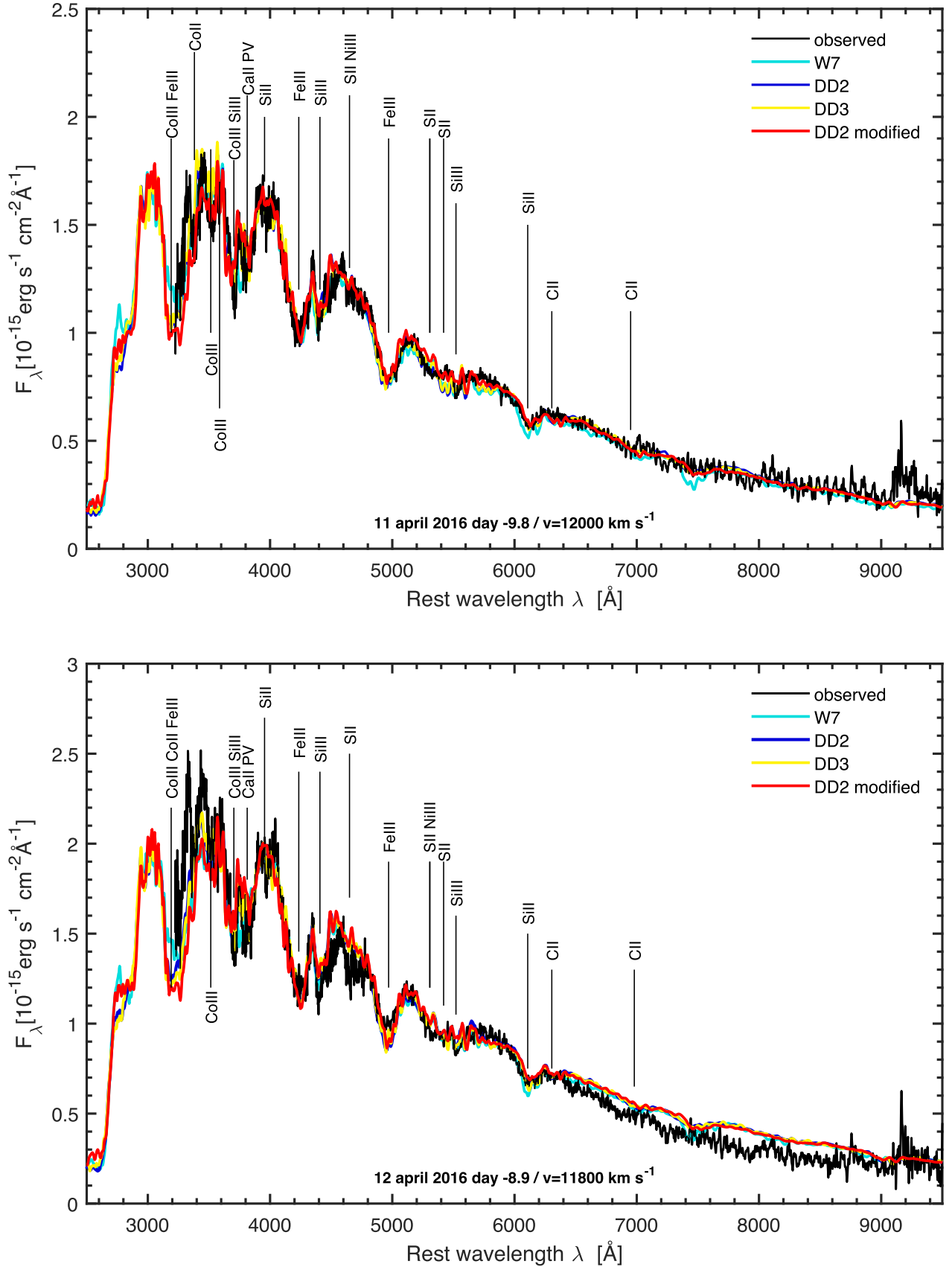


Figure 6. Observed early spectra of iPTF16abc (black), compared to the synthetic spectra in colours, corresponding to different density profiles as indicated in the legend. Epochs are shown with reference to B maximum.

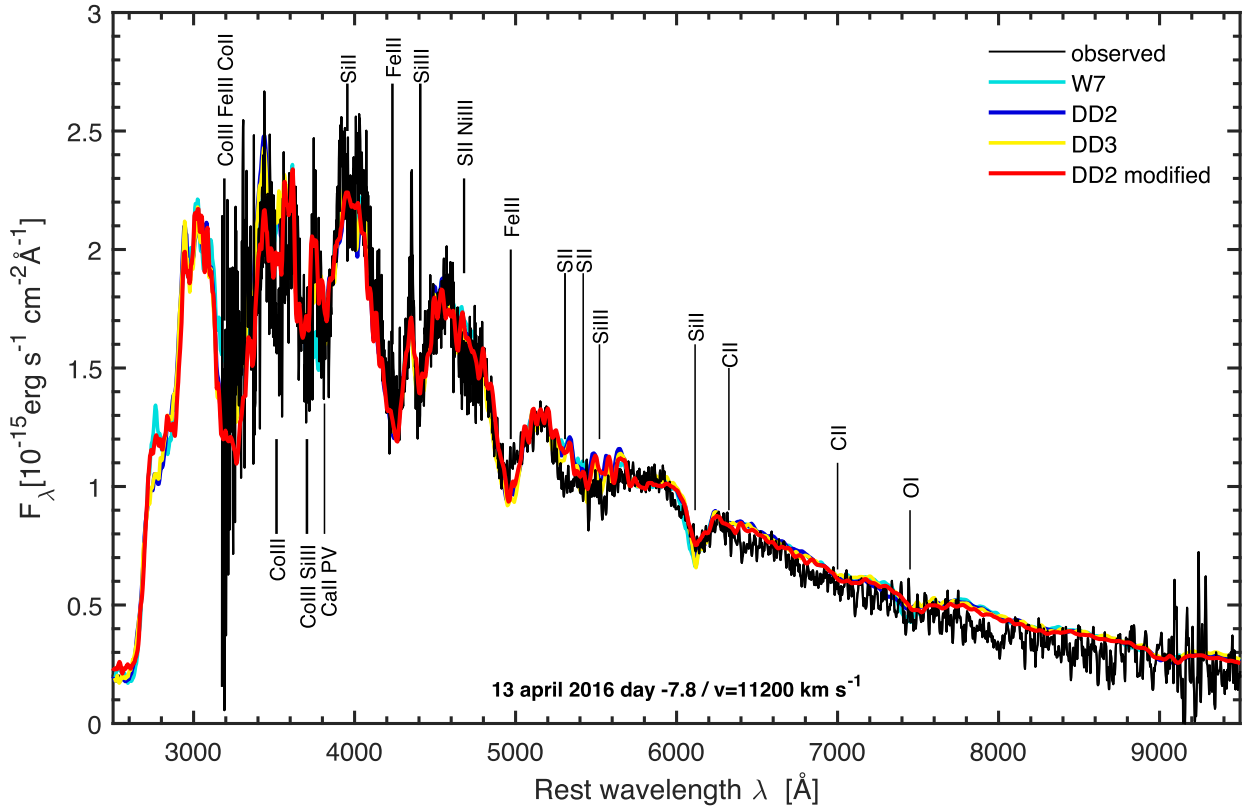


Figure 7. Observed day -8 spectrum of iPTF16abc (black), compared to the synthetic spectra in colours, corresponding to different density profiles as indicated in the legend. Epoch is shown with reference to B maximum.

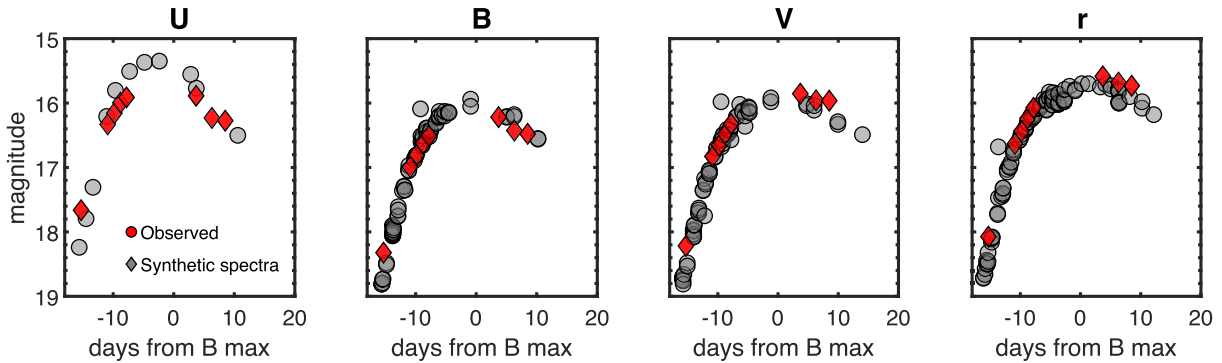


Figure 8. Light curves from observation compared to the ones from synthetic spectra. Photometry data from Miller et al. (2018).

velocity at $v > 13450 \text{ km s}^{-1}$. This adjustment yields negligible differences compared to the spectrum containing calcium and shows the dominance of Si III and Co III. In contrast, SN 1999aa distinctly displays Ca II dominance in the same feature during the same period, an influence even more pronounced in SN 2003du.

By day -8 , a calcium mass fraction of 0.005 is sufficient for our synthetic spectra. These values fall within the range computed for SNe 1999aa and 1991T, but are significantly lower than the values reported for the spectroscopically normal events (Tanaka et al. 2008, 2011).

The presence of free electrons in the outer shells can affect the Ca II H&K HV feature's strength by promoting recombination from Ca III to Ca II, which may support the presence of hydrogen as discussed by Mazzali et al. (2005). This allows for various calcium and hydrogen

fractions combinations to reproduce the line, as shown by Aouad et al. (2022). In the case of iPTF16abc, a significant hydrogen mass fraction (up to 0.05) would be needed to noticeably change the calcium ionization state. This quantity produces observable hydrogen lines like $H\alpha$, which are absent in the spectra. Thus, the derived calcium mass fraction can be considered reliable.

The Ca II near-infrared (NIR) feature, typically observed in normal SNe Ia, is notably absent in the early spectra of iPTF16abc and only becomes visible a few days after maximum brightness. This behaviour resembles SNe 1999aa and 1991T and is reproduced well in our synthetic spectra.

Silicon, Sulphur, Magnesium: The Si II $\lambda 6355$ feature is barely noticeable in the day -15 spectrum but gains slight strength on days -11 and -10 , resembling SN 1999aa at the same epoch. Conversely,

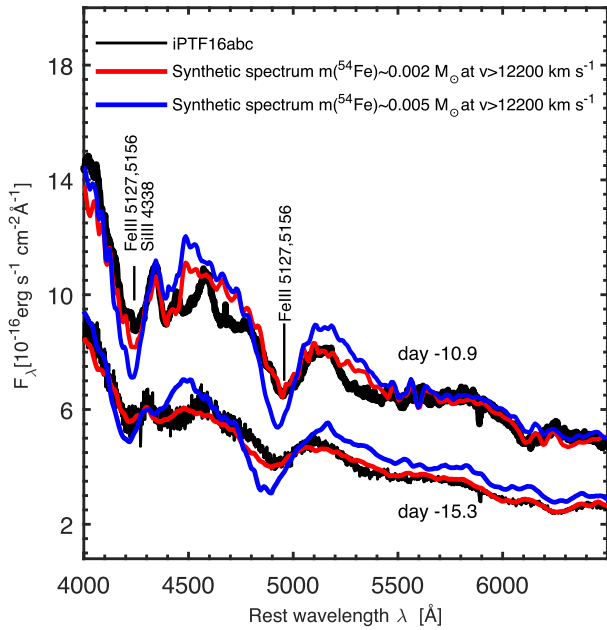


Figure 9. Probing iron at the outermost layers. The blue spectra are models generated replicating an iron abundance similar to SN 1999aa [$X(\text{Fe}) = 0.018$ at $v > 12\,200\text{ km s}^{-1}$, with a total mass of $0.005 M_{\odot}$ (Aouad et al. 2022)]. The red spectra have been produced using $X(\text{Fe}) = 0.00035$ at $v > 13\,450\text{ km s}^{-1}$, and $X(\text{Fe}) = 0.025$ in the shell above $12\,200\text{ km s}^{-1}$, with a total mass of $0.002 M_{\odot}$. Notably, despite the outermost shells of iPTF16abc exhibiting supersolar abundances, its iron content in these layers remains lower than that of both SNe 1999aa and 1991T. Epochs are shown with reference to B maximum.

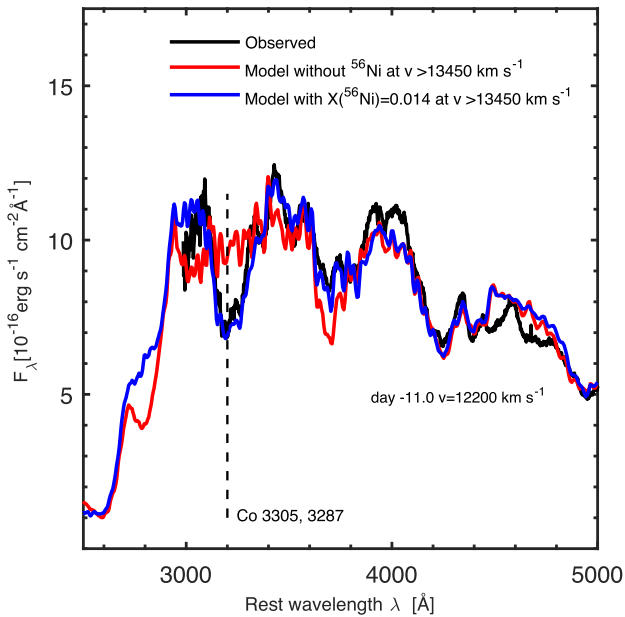


Figure 10. Probing nickel at the outermost layers. A ^{56}Ni mass fraction of 0.014 is required at the outermost shell at $v > 13\,450\text{ km s}^{-1}$ to replicate the $\text{Co III } \lambda\lambda\ 3287, 3305$ line observed near 3200 \AA . Epoch is shown with reference to B maximum.

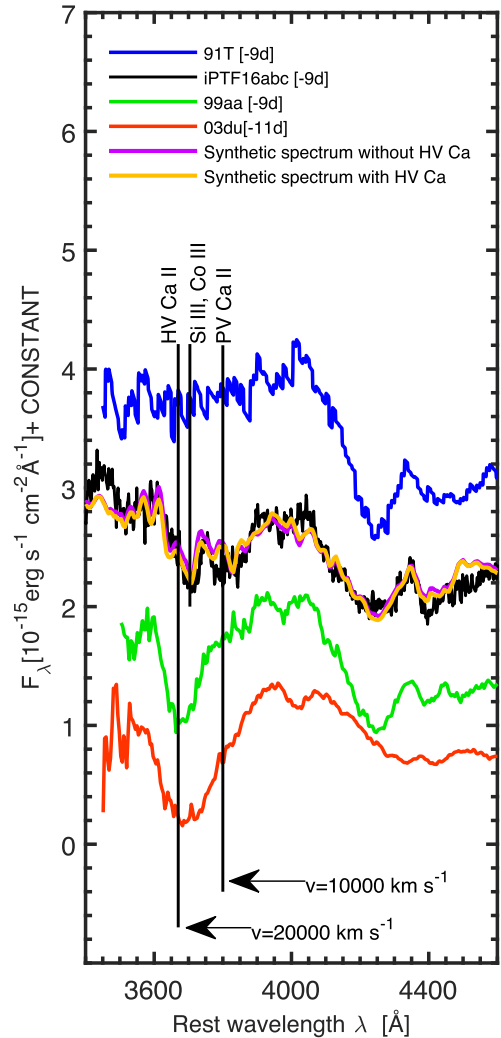


Figure 11. Detail of the region around $\sim 3700\text{ \AA}$, the HV Ca II feature reveals a split into two components. The bluer portion is characterized by the influence of Si III and Co III rather than Ca II in iPTF16abc. Interestingly, a synthetic spectrum at day -9 , lacking calcium at high velocity ($X(\text{Ca}) = 0 > 13\,450\text{ km s}^{-1}$), shows no discernible difference in its bluer segment compared to the one featuring Ca. In contrast, in SN 1999aa, Ca II dominates the same feature at the same time, and this dominance is even more pronounced in SN 2003du. Epochs are shown in square brackets with reference to B maximum.

the Si III $\lambda\ 4560$ feature is strong and increases in intensity as the spectra evolve. To match these features, a Si mass fraction of 0.013 is required at $v > 13\,450\text{ km s}^{-1}$, on day -15 . Higher Si fractions would produce stronger features than observed (cf. Fig. 12). On day -11 , the Si mass fraction sharply rises to 0.47 at $v > 12\,200\text{ km s}^{-1}$, before gradually decreasing inward. The precise matching of the line ratios between Si II and Si III features in our synthetic spectra indicates a well-constrained ionization balance and therefore temperatures in our models.

The two S II $\lambda\lambda\ 5468, 5654$ lines begin to appear on day -10 , and our synthetic spectra reasonably replicate their depth and evolution. The sulfur mass fraction follows a similar trend to silicon. The depletion of intermediate-mass elements in the velocity range of $\sim 12\,000\text{--}13\,000\text{ km s}^{-1}$ is akin to what has been suggested for SNe

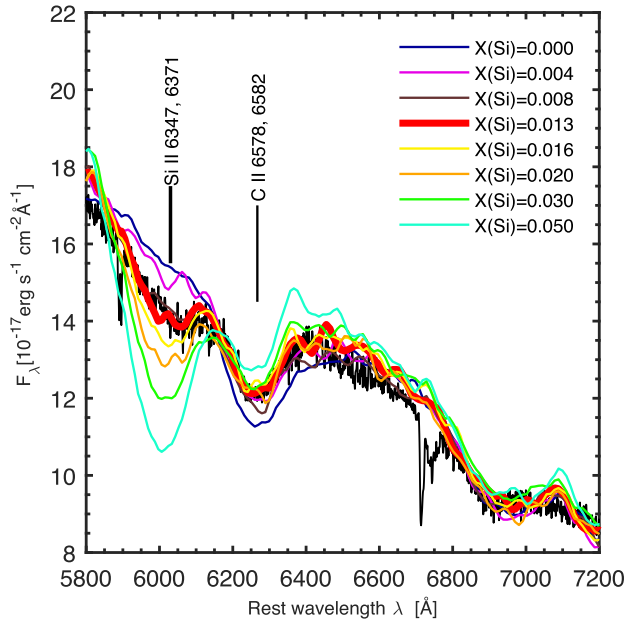


Figure 12. Probing silicon in the outer layers. The optimal replication of the Si II λ 6355 absorption line observed on day -15 with reference to B maximum is attained with a silicon mass fraction of 0.013 at velocities $v > 13\,450$ km s^{-1} . The observed spectrum is represented in black, and models with varying silicone fractions are depicted in different colours as indicated in the legend.

1999aa and 1991T, contrasting with spectroscopically normal SNe Ia (Aouad et al. 2022).

The contribution of Mg to the line near 4200 Å is not significant, as this line is primarily dominated by Fe III, resembling what was observed in SNe 1999aa and 1991T. We consider a Mg mass fraction of 0.01 at $v > 13\,450$ km s^{-1} .

Carbon, Oxygen: A strong C II λ 6580 and a weaker C II λ 7234, are evident in the day -15 spectrum. They diminish as time progresses but surprisingly re-emerge at day $+3.7$, gaining strength by day $+8$. To accurately replicate these C II features, a mass fraction of 0.007 is required at $v > 13\,450$ km s^{-1} , (day -15 , cf. Fig. 13) decreasing to 0.005 at $v > 11\,200$ km s^{-1} on day $+8$.

Notably, clear carbon lines are not unambiguously present in the spectra of SNe 1999aa and 1991T. Upper limits of 0.0005 and 0.005 were, respectively, reported in a velocity range of 12 500–17 000 km s^{-1} , (Saselli et al. 2014; Aouad et al. 2022), while Tanaka et al. (2011) noted a mass fraction of 0.002 for the normal SN 2003du at $10\,500 < v < 15\,000$ km s^{-1} . The absence of carbon detection in SNe Ia may stem from observational biases such as the lack of early spectra or line blending. Nevertheless, it has been reported in a significant fraction of SNe Ia across all spectroscopic classifications (Parrent et al. 2011; Folatelli et al. 2012).

Our synthetic spectra reproduce an O I λ 7771 line near 7400 Å, which is absent in the observed spectrum at day -15 . The formation of this line has also been reported in previous works (Tanaka et al. 2011; Aouad et al. 2022). During this specific epoch and within this velocity range ($13\,500$ km $s^{-1} < v < 14\,000$ km s^{-1}), the density in our models drops to $\log \rho \approx -12.2$ g cm^{-3} , while the radiation temperature reaches approximately 10^4 K. Under these conditions, the Sobolev optical depth for the O I λ 7771 line surpasses unity, leading to the formation of this spectral feature. The removal of this line from the models necessitates either substituting oxygen with alternative elements, which could introduce unobserved features in

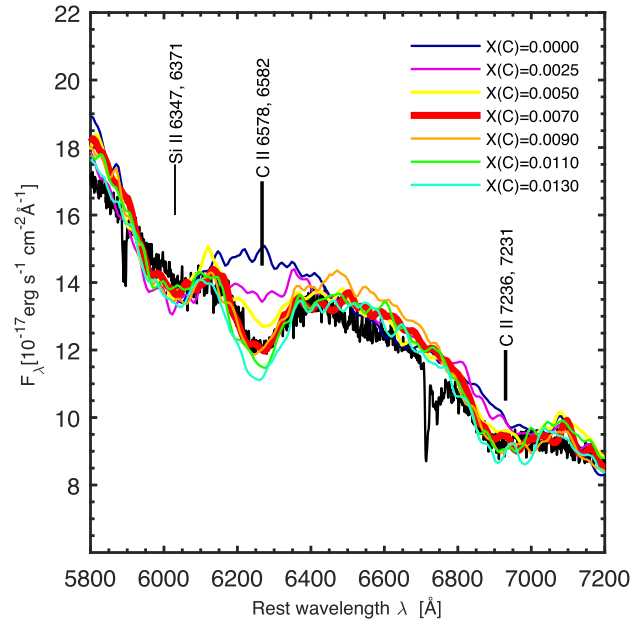


Figure 13. Probing carbon in the outermost layers. A carbon mass fraction of 0.007 provides the most accurate reproduction of the two primary C II features observed on day -15 with reference to B maximum at velocities $v > 13\,450$ km s^{-1} . (The observed spectrum is shown in black, and models with different carbon mass fractions are illustrated in various colours as indicated in the legend.)

the spectra, and furthermore is difficult to explain in the context of Ia's. Or it requires much high temperatures, which would alter the ionization balance and hinder the formation of other spectral lines. Another avenue to explore is the possibility of density reduction in the outermost layers, a topic we investigate further in Section 5. In any case, with a mass fraction of 0.94, oxygen prevails at $v > 13\,450$ km s^{-1} , but decreases inward, as the composition becomes dominated by other elements, which are needed to replicate the spectral features.

The absorption line near 6300 Å has been attributed to H α in previous studies (Lentz et al. 2002), but our synthetic spectra could not reproduce accurately this line using H, at any velocity. More importantly, replacing C with H will not allow for the appearance of C II λ 7234 clearly seen and accurately replicated on day -15 .

4.2 Post-maximum spectra

Figs 14 and 15 show spectra from 3.7 to 8.5 days after B maximum. At this epoch, the photosphere resides inside the ^{56}Ni dominated shell. Consequently, the assumption of a well-defined photosphere becomes less precise, and a substantial portion of the radiation energy is deposited above the photosphere in reality. This and the assumption of blackbody radiation at the photosphere may cause the excess flux at the redder wavelengths beyond ~ 6000 Å in the models. However, this supposedly does not strongly affect line formation or the ionization balance in our models.

Fe-group elements: At this epoch, several Fe II lines start to form and influence the main Fe dominated feature near 4800 Å. The Fe II lines are accurately replicated and their ratio to Fe III lines is faithfully reproduced in our synthetic spectra, indicating that our models are still in good ionization balance. From day $+3.7$ until day $+6.3$, the stable Fe mass fraction stabilizes at 0.05, constituting ~ 30 per cent

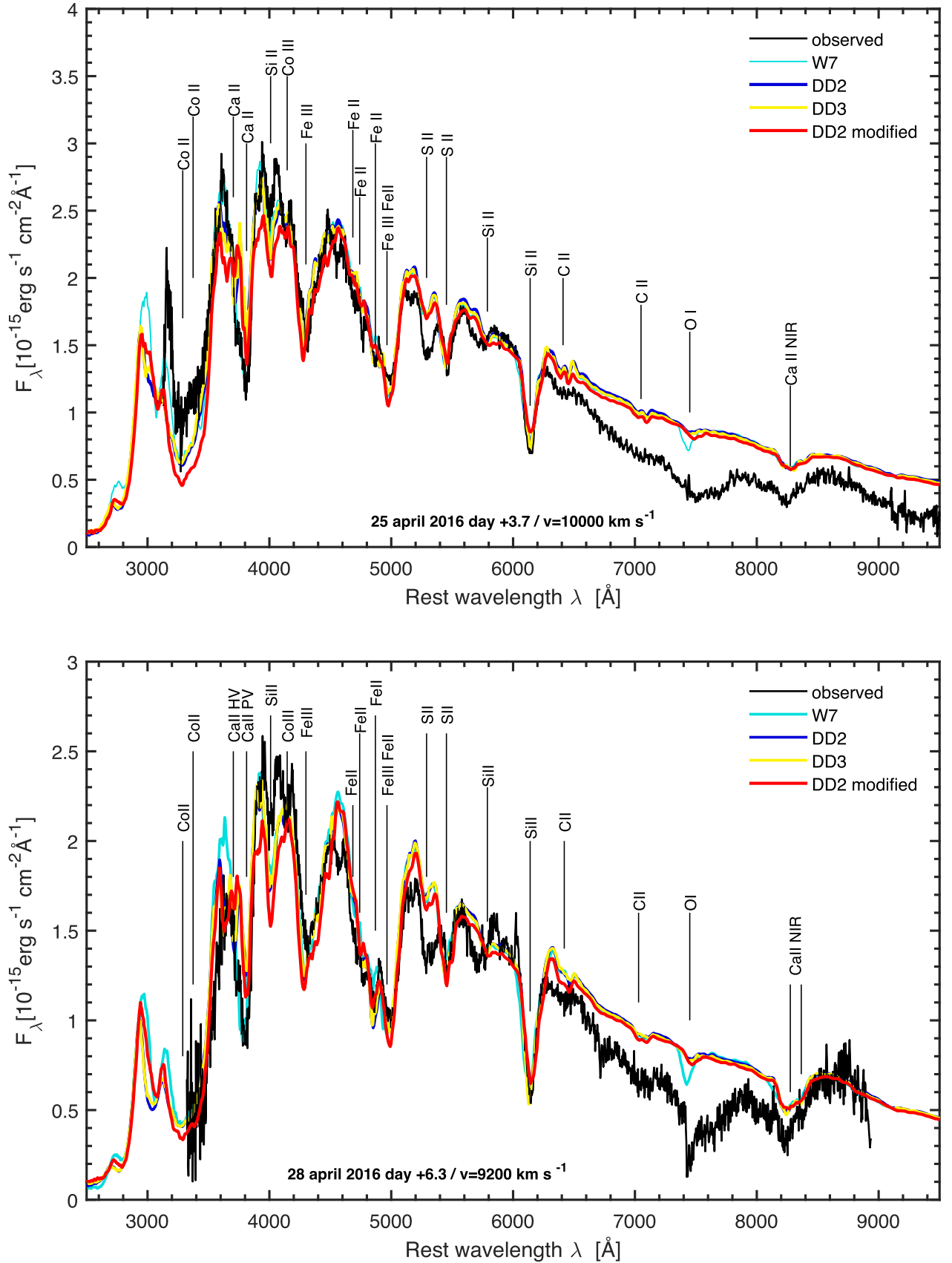


Figure 14. Comparison of post-maximum observed spectra of iPTF16abc (black) with synthetic spectra in various colours, corresponding to different density profiles as specified in the legend. Features near 6780 (weak) and 7400 Å (strong) are telluric. Epochs are presented with reference to B maximum.

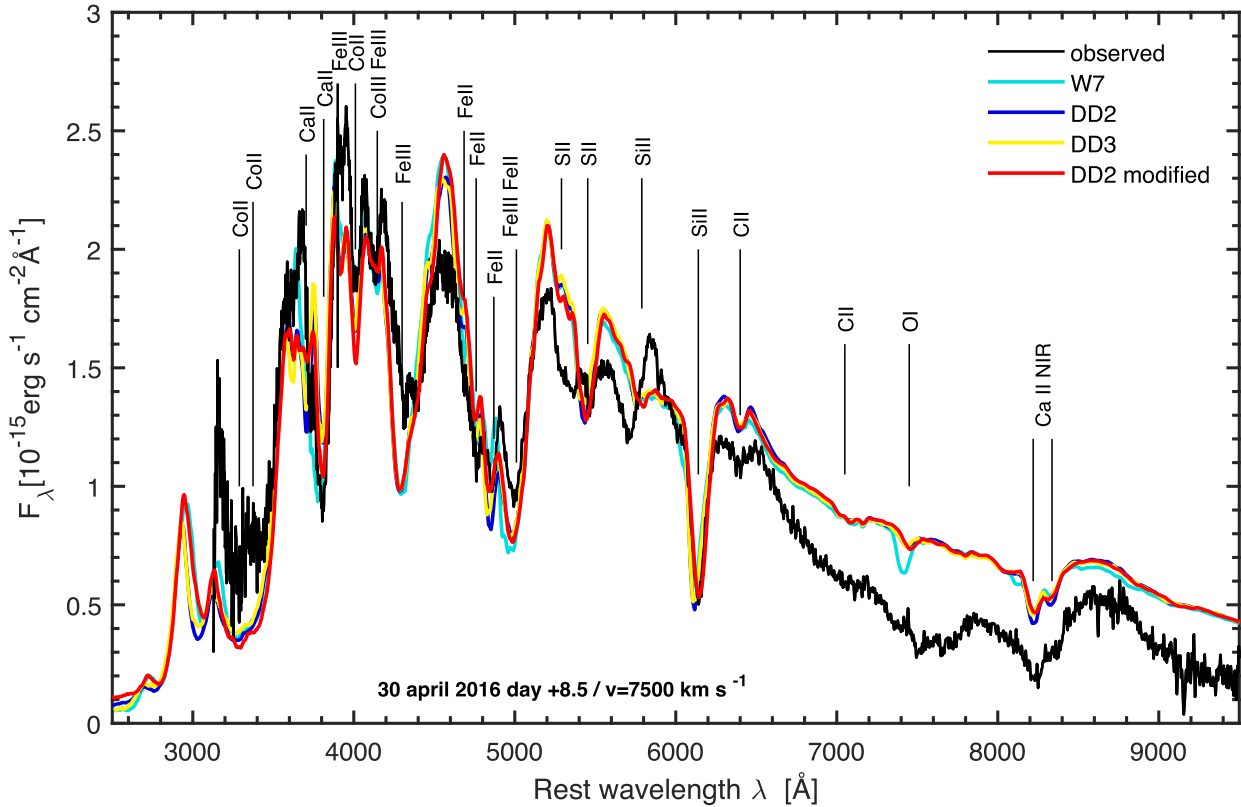


Figure 15. Comparison of day +8 observed spectrum of iPTF16abc (black) with synthetic spectra in various colours, corresponding to different density profiles as specified in the legend. Epochs are presented with reference to *B* maximum.

of the total iron content, while the remaining iron originates from the decay of ^{56}Ni . By day +8.5, this fraction increases to 0.3, which is necessary to replicate the emission lines present in the nebular phase spectrum (cf. Section 6).

The ^{56}Ni mass fraction remains 0.69 in the probed shells until day +8.5. The feature near 4000 Å, earlier due to Si II λ 4130, becomes fully dominated by Co II λ 4160 at day +8.5. A blend of Co III $\lambda\lambda$ 4317, 4249 and Fe III λ 4352, create a feature near 4150 Å, which is also accurately replicated in our synthetic spectra. The deep feature observed near 3200 Å previously dominated by Co III $\lambda\lambda$ 3305, 3287 is now dominated by a blend of Co II lines as the temperature drops and the ionization balance shifts towards singly ionized species.

Calcium: The Ca II NIR appears around day +3.7. This feature clearly splits into two different components at day +6.3 and after, which is accurately replicated. The Si III and Co III contributions to the feature near 3800 Å reduce with time until it is dominated by Ca II H&K, with a significant contribution of Si II λ 3858 (Childress et al. 2014). This is expected as the temperatures drop. This feature is better reproduced with the W7 density profile. This may be due to the density bump in the W7 profile in the velocity shell between 13 000 and 16 000 km s^{-1} , where the PV component of the line forms. The Ca mass fraction needed decreases from 0.005 at day +3.7 to 0.001 at day +8.5 at $v > 7500 \text{ km s}^{-1}$.

Silicon, Sulphur: At this epoch, the prominent feature near 4400 Å earlier due to Si III $\lambda\lambda$ 4552, 4567, 4574 becomes fully dominated by a blend of Fe III $\lambda\lambda$ 4420, 4431, 4395, and a Co III λ 4433 lines. As a result, the two separated features at 4200 and 4400 Å earlier seen in the pre-maximum epochs, blend into one deep absorption feature, which is accurately replicated. This is common

to all type Ia that we have modelled (cf. Tanaka et al. 2011; Sasdelli et al. 2014; Aouad et al. 2022). The Si II λ 6355 gets deeper as the spectra evolve. The Si II λ 5972 line appears at day +3.7 as depicted in our synthetic spectra. At day +6.3, the Si fraction is 0.17. At $v < 7500 \text{ km s}^{-1}$, ^{56}Ni and stable iron dominate the abundance.

Carbon, Oxygen: The carbon mass fraction increases from 0.005 at $v > 11 200 \text{ km s}^{-1}$, to 0.03 at $v > 10 000 \text{ km s}^{-1}$, to slightly decrease to 0.025 at $v > 9200 \text{ km s}^{-1}$. The overall increase over the shells between 9200 and 11 800 km s^{-1} (cf. Fig. 22), is essential to replicate the C II λ 6580 at days +3.7, +6.3, and +8.5. Notably, there is no requirement for carbon presence below 9200 km s^{-1} , as any carbon abundance at this velocity would shift the line to the red, deviating from its observed position (cf. Fig. 16). At day +8.5, the velocity of the C II line is $\sim 8000, 500 \text{ km s}^{-1}$ detached above the photosphere ($v_{\text{ph}} = 7500 \text{ km s}^{-1}$). As oxygen cannot be accurately constrained from any visible line in the spectra, a similar abundance as carbon is assumed since it is difficult to justify the presence of carbon without oxygen.

5 A MODIFIED DENSITY PROFILE

Our primary motivation for exploring modifications to the density profile arises from the presence of the O I λ 7771 line in our models using DD2, DD3, and W7 density profiles, which is absent in the data obtained from the earliest spectrum taken at day -15. To address this, we experiment with modifying the original DD2 density profile. We find that the most favourable outcome is achieved by removing 0.05 M_{\odot} of mass at $v > 13 450 \text{ km s}^{-1}$, while simultaneously adding the missing mass in the deeper layers. This ensures the conservation

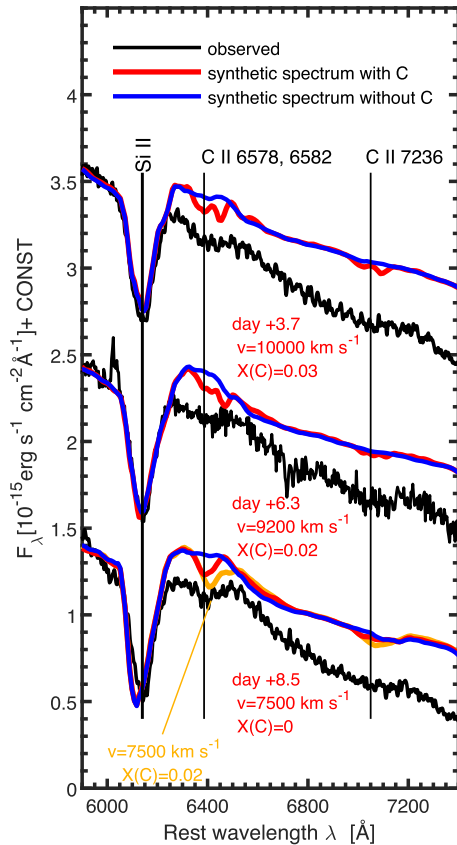


Figure 16. Probing carbon at the inner layers: spectra taken approximately 4 to 8 days after the peak. To accurately replicate the observed feature at around 6400 Å, carbon presence is required down to velocities as low as $v = 9200 \text{ km s}^{-1}$. Introducing carbon at even lower velocities would cause the absorption line to shift redder from its observed position, as depicted in the yellow synthetic spectrum generated at day +8.5. Epochs are presented with reference to B maximum.

of the total mass, while the total kinetic energy is not significantly affected due to the small mass shift (cf. Fig. 4). This approach has already been used in Hachinger et al. (2009), Ashall et al. (2016), and in Mazzali et al. (2014). This minor modification does not substantially affect the abundance as a function of velocity neither the integrated yields. Attention has been given to avoid steep density gradients. Such gradients might trigger the formation of lines within narrower velocity ranges, thus potentially yielding lines significantly narrower than those observed. The results are shown in Figs 5, 6, 7, 14, and 15 with red lines. Notably, the manipulation of the density profile had minimal visible impact on most lines, but it reduced the O I signature substantially. Removing more mass from the outer layers will eventually affect the formation of other lines.

In general, all density profiles we used yield reasonably good fits to the observed spectra, which makes it difficult to favour any one model. The same result was obtained when modelling SN 1999aa. Upon closer examination, both DD models exhibit a striking resemblance and outperform the W7 model in certain spectral regions, such as the vicinity of 3800 Å during the pre-maximum epoch, whereas W7 performs better in the same region during the post maximum epoch. The W7 model consistently generates a narrow and robust O I λ 7771 line, even in post-maximum spectra. The modified DD2, despite wiping out the strong O I λ 7771 in the earliest spectrum, falls short in reproducing the Si II λ 6355 line in the post maximum spectra

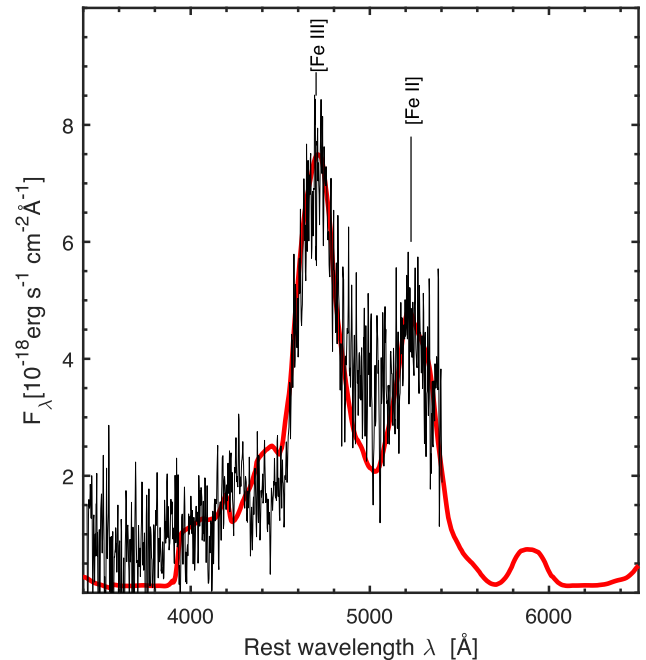


Figure 17. Nebular spectrum of iPTF16abc on day +342 with reference to B maximum light, displayed in black, compared with our synthetic spectrum in red.

at days +3.7 and +6.3. Also the model does not reach the peak flux around 4000 Å. Therefore, we deduce that the delayed detonation models appear to be reasonable, although they may necessitate some adjustments in line with the conclusions drawn for SN 1999aa (Aouad et al. 2022). Our inclination towards DD models is also substantiated by insights gained from the abundance distribution and the total ^{56}Ni content, which we explore in greater detail in Section 7.

6 THE NEBULAR PHASE

Modelling the nebular spectrum allows us to derive the properties of the inner ejecta. Nebular spectra of SNe Ia are dominated by forbidden lines of [Fe II] and [Fe III] in emission and usually display lines of a few other elements, such as Mg and Ca (e.g. Mazzali et al. 2008). The emission intensity is a diagnostic for the content of ^{56}Ni . Most ^{56}Ni in SNe Ia is normally located at low velocity, and so the nebular phase is the best time to see it directly. At the typical epochs of nebular spectra (~ 1 year), most ^{56}Ni has decayed into ^{56}Fe . The residual ^{56}Co still heats the gas upon decaying into ^{56}Fe , and this is balanced by cooling via line emission. Computing the heating rate and balancing this with cooling yields an estimate of the mass of ^{56}Ni synthesized in the explosion, as well as the overall mass and composition of the emitting region, which is usually confined to the region where the abundance of ^{56}Ni is high. Additionally, the presence of lines of two different ions of iron, Fe II and Fe III, is very useful in order to estimate the recombination rate, and hence the density of the gas. The ionization balance is affected by additional cooling provided by the stable iron atoms that are also synthesized during explosive burning if the density is sufficiently high. Estimating the mass of stable Fe is a powerful tool to estimate the mass of the progenitor white dwarf at the time of explosion, and ultimately to differentiate between different explosion scenarios, as stable Fe is

thought to be synthesized only if the white dwarf has a mass close to the Chandrasekhar limit.

Unfortunately, the nebular spectrum for iPTF16abc at day +342.4 has limited wavelength coverage and low signal-to-noise ratio. Furthermore, no photometric measurements are available at this epoch. In order to calibrate the spectrum, we extrapolated the *g*-band photometry measurement from a few days earlier. Additionally, we used the $U - g$ colour of a similar supernova, SN 1999aa, as an approximation to calibrate the U -band. While this approach is rudimentary and susceptible to potential inaccuracies, it can still yield results that fall within ≈ 20 percent of the true ones. Consequently, there is some uncertainty associated with the derived ^{56}Ni mass. However, these quantities are subjected to further validation against the bolometric light curve, which we explore in Section 8.

The available nebular spectrum of iPTF16abc was modelled (cf. Fig. 17) with our SN nebular code (see Fig. 17) (Mazzali et al. 2001b). The code computes the deposition of the γ -rays and positrons produced by ^{56}Ni and ^{56}Co decay using a Monte Carlo scheme (Cappellaro et al. 1997) and balances the heating that this causes with cooling via emission lines in non-local thermodynamic equilibrium (NLTE), following the principles laid out in Axelrod (1980). The best-fitting density profile, WDD2, was used for our models, together with the outer layers' composition determined by photospheric-epoch spectral fitting above. The composition in the inner layers, which are only visible at late times, was determined by modelling the nebular spectrum itself. These inner layers are dominated by Fe-group elements. ^{56}Ni was introduced until a flux was reached that was comparable to the observed one. Unfortunately, the nebular-phase spectrum of iPTF16abc does not extend far enough to the red for us to be able to estimate the mass of calcium, which is an important coolant despite its typically low abundance. This introduces some uncertainty into our results.

7 ABUNDANCE TOMOGRAPHY

Using the results of both the photospheric and the nebular phases, we construct the abundance as a function of depth. This is shown in Fig. 18, where we plot the mass fraction of the main elements as a function of velocity and mass compared to the original abundance profile of the DD2 hydrodynamic model (Iwamoto et al. 1999).

The inner core, up to about 3500 km s^{-1} , is dominated by neutron rich stable iron group elements. The nucleus that prevails within the innermost layer is ^{58}Ni , but our calculations indicate its depletion occurring at 1000 km s^{-1} . In contrast, in the original model, ^{58}Ni persists much farther outward. This consistent finding was observed in all the events we modelled. Recently, stable IGEs have been confidently detected in *JWST* spectra of normal SNe Ia (DerKacy et al. 2023), further supporting the results of our modelling. Situated above this, ^{58}Ni -dominated layer is a layer primarily composed of stable iron (i.e. ^{54}Fe), which extends until 3500 km s^{-1} .

In the shell spanning from 5000 to $\approx 12\,500 \text{ km s}^{-1}$, ^{56}Ni emerges as the dominant nucleus with a combined mass of $\sim 0.76 M_{\odot}$, accompanied by a portion of stable iron. Unlike the high-density inner shells, these outer shells remain unaffected by electron capture but instead undergo complete Si burning, aligning with the original hydrodynamic model. As we progress outward, the density gradually decreases, hindering the achievement of complete Si burning. Consequently, the quantity of Ni gradually diminishes, making way for IMEs, with Si and S being the primary species, accompanied with a portion of Ca. The abundance profile of this IMEs shell is similar to the hydrodynamical model, exhibiting a gradual increase as the abundance of ^{56}Ni starts to decrease.

However, contrary to the original model, our calculations reveal that the Si abundance peaks at $\approx 12\,500 \text{ km s}^{-1}$ and experiences sudden depletion at $v > 13\,400 \text{ km s}^{-1}$. Consequently, the Si-rich layer occupies a narrower velocity range than in the original model, where it extends out to $v = 17\,500 \text{ km s}^{-1}$. This bears a striking resemblance to the behaviour observed in SNe 1999aa and 1991T, suggesting a similar explosion mechanism (Sasdehli et al. 2014; Aouad et al. 2022). This is further supported by the abrupt increase in oxygen abundance prevailing in the outermost layers beyond $15\,000 \text{ km s}^{-1}$. Interestingly, carbon is present in the shells dominated by Si and unexpectedly extends and increases inwards until about 9200 km s^{-1} . It is difficult to explain the increase of C abundance at these deep shells with conventional symmetric explosion models. Unburned carbon is typically expected at $v \gtrsim 15\,000 \text{ km s}^{-1}$, in the W7 model and even higher velocities in the DD models (Nomoto et al. 1984; Iwamoto et al. 1999). Diverging from established explosion models, ^{56}Ni and stable iron are both present in the outermost layers until $v = 25\,000 \text{ km s}^{-1}$, albeit at percentage level.

The integrated yields from our results are shown in Table 2. Using these values, we compute the total kinetic energy using the formula

$$E_k = [1.56M(^{56}\text{Ni}) + 1.74M(\text{NSE}) + 1.24M(\text{IME}) - 0.46] \times 10^{51} \text{ ergs} \quad (1)$$

(Woosley et al. 2007), where $M(^{56}\text{Ni})$, $M(\text{NSE})$, and $M(\text{IME})$ correspond to the ejected mass of ^{56}Ni , nuclear statistical equilibrium elements, and IMEs, respectively. This yields a value of $1.32 \times 10^{51} \text{ ergs}$. The ^{56}Ni mass closely resembles that of the original DD3 model. However, the kinetic energy falls slightly short when compared to both the DD2 and the DD3 models (cf. Table 2). This outcome is expected due to the insufficient presence of IMEs, which is not adequately compensated for by an increase in ^{56}Ni production. This is a common trait for all the 91T-like we have modelled. Interestingly, when we assess the mass ratio IMEs/IGEs, the 91T-like objects exhibit a common value (Table 2 and in Fig. 19), which is notably lower than that of both the normal events and the hydrodynamical models. The IGEs mass of $\sim 0.2 M_{\odot}$ is in the range expected for all SNe Ia (Mazzali et al. 2007). We estimate the mass of carbon to be $\sim 0.01 M_{\odot}$ above 9200 km s^{-1} , which aligns with the expected range of 0.001 to $0.01 M_{\odot}$, as reported by Folatelli et al. (2012). In general, the abundance distribution more closely resembles delayed detonation models. Explaining the extension of the ^{56}Ni -dominated shell this far out in the ejecta using the W7 model proves challenging, especially considering that the total ^{56}Ni mass suggested from our modelling surpasses the total ^{56}Ni mass anticipated from the W7 model.

8 BOLOMETRIC LIGHT CURVE

We generate a bolometric light curve spanning 3000 – $10\,000 \text{ \AA}$, (cf. Fig. 20) utilizing the *UBVri* photometry data reported in Miller et al. (2018). This will then be compared to a light curve computed from our model (cf. Section 8.1). In cases where multiple photometric measurements were available for a given epoch, we calculate the average magnitude; this introduces an error of $\sim 0.1 \text{ mag}$. U band photometry data are not available beyond day +22 from B maximum light. Therefore, for these epochs, we assume U band measurements by applying a constant $U - B$ value as computed from the last epoch, where these two measurements were available (i.e. day +21). Next, we interpolate the data at a daily resolution and convert the magnitudes to fluxes by applying the flux zero-points of Fukugita, Shimasaku & Ichikawa (1995), dereddened with the extinction curve

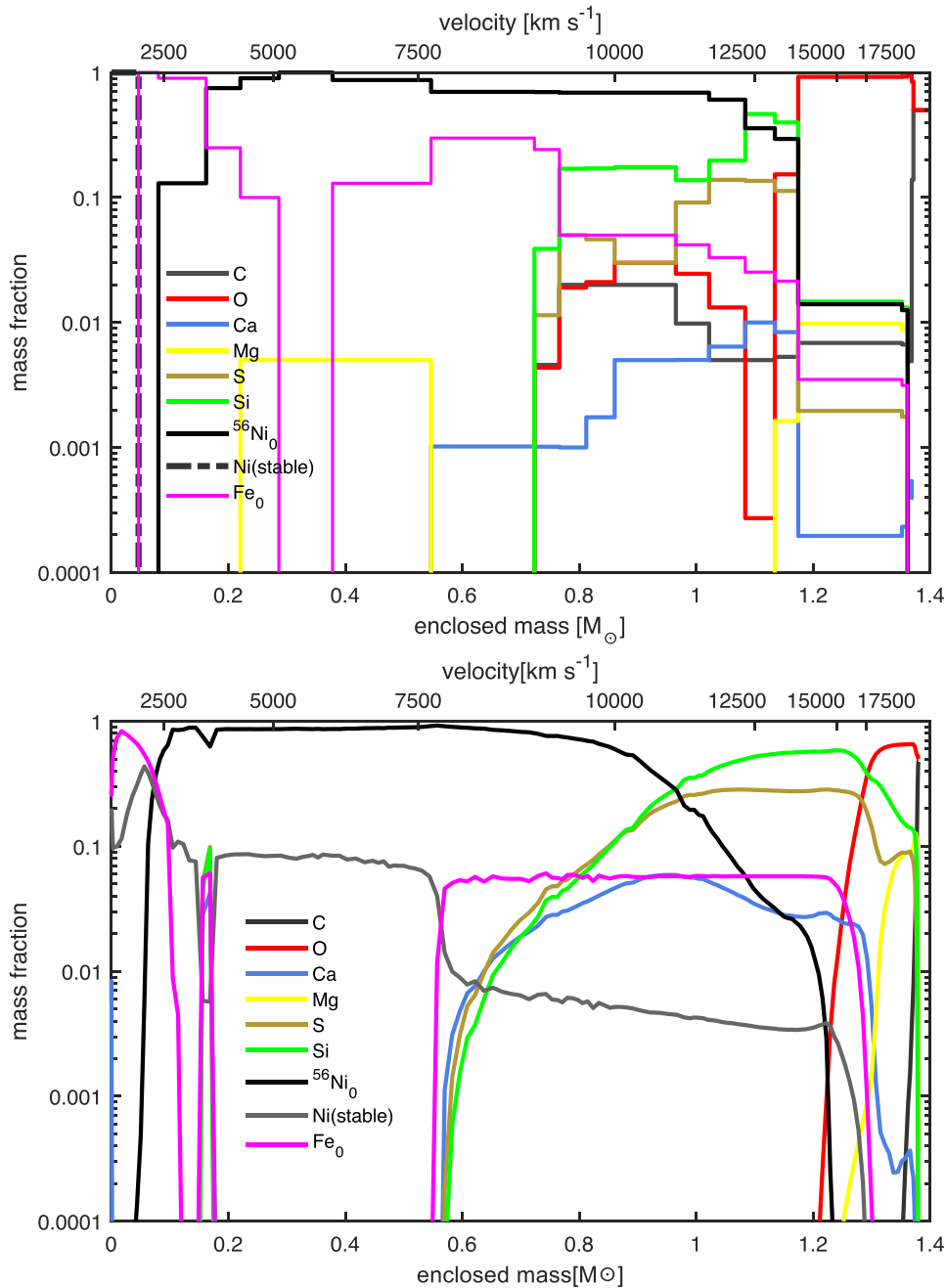


Figure 18. Upper panel: abundances obtained from spectral models using the DD3 density profile. Lower panel: the original nucleosynthesis from DD3 (Iwamoto et al. 1999).

of Cardelli, Clayton & Mathis (1989) using $E(B - V) = 0.08$ mag (Miller et al. 2018). For each epoch, we compute the flux via trapezoidal integration between the specific flux values obtained at the central wavelength of each passband. We extrapolate the spectrum with a linearly decreasing function until 3000 and 10000 Å to extend the flux calculation beyond the U and i band central wavelengths. Finally, we compute the bolometric luminosities using the adopted distance modulus of 35.01 considering an error of 0.15 mag (Makarov et al. 2014).

The supernova exhibited its highest luminosity, measuring $L_{\text{peak}} = 1.60 \pm 0.1 \times 10^{43}$ ergs s⁻¹, with a rise time of 18.74 d in the supernova

rest frame. The bolometric peak was observed to occur roughly one day prior to B_{max} , which is in line with previous studies examining bolometric rise time (Contardo, Leibundgut & Vacca 2000; Scalzo et al. 2012).

Miller et al. (2018) reported a bolometric peak of $1.2 \pm 0.1 \times 10^{43}$ for iPTF16abc using a distance modulus of 34.89 ± 0.10 mag. We adopted a distance modulus of 35.01 mag, consistent with our modelling. Using a shorter distance would require a smaller luminosity input, which in turn would not reproduce the ionization balance found in our models. Even if we use the distance from Miller et al. (2018), it would result in a bolometric peak

Table 2. Nucleosynthetic yields and kinetic energies from the modelling compared to the original hydrodynamic models. Results from other SNe are also shown. E_k for models is calculated using equation (1) in the text.

	^{56}Ni	Fe ^a	Ni _{stable}	IME ^b	O	IME/IGE	E_k
	M_\odot	M_\odot	M_\odot	M_\odot	M_\odot		10^{51} ergs
iPTF16abc (DD2)	0.76	0.20	0.006	0.19	0.21	0.197	1.32
original W7	0.59	0.16	0.122	0.24	0.143	0.275	1.30
original DD2	0.69	0.10	0.054	0.33	0.066	0.39	1.40
original DD3	0.77	0.10	0.0664	0.25	0.056	0.27	1.43
1991T (DD3)	0.78	0.15	0.0006	0.18	0.29	0.19	1.24
1999aa (DD2)	0.65	0.29	0.006	0.20	0.22	0.21	1.32
2003du (W7)	0.62	0.18	0.024	0.26	0.23	0.32	1.25
2002bo (W7)	0.49	0.27	0.0001	0.28	0.11	0.37	1.24
2004eo (W7)	0.32	0.29	0.0005	0.43	0.3	0.70	1.1

Notes. ^aAll stable isotopes except for ^{56}Fe , decay product of ^{56}Ni
^b $^{28}\text{Si} + ^{32}\text{S}$

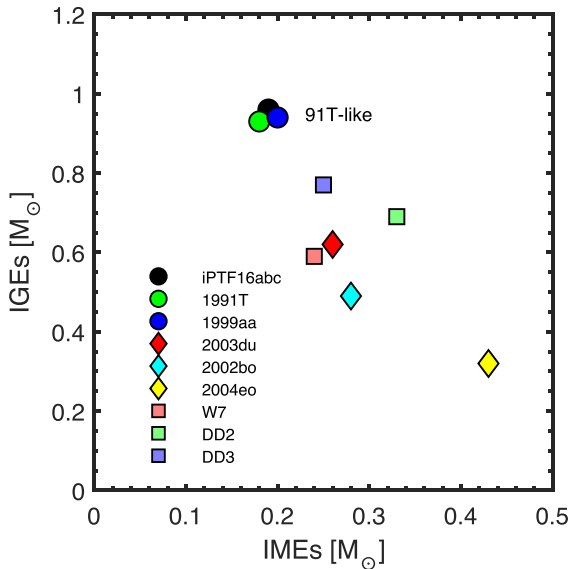


Figure 19. Scatter plot showing the total mass of Intermediate Mass Elements (IMEs) plotted against the total mass of Iron Group Elements (IGEs) for iPTF16abc as computed from our modelling, compared to other SNe and explosion models. Notably, the 91T-like events are observed to occupy a distinct region within this space.

of $1.48 \pm 0.1 \times 10^{43}$, still more luminous than SN 1999aa and closer to SN 1991T, consistent with observations of their spectra. Additionally, our computed bolometric luminosities from synthetic spectra align well with both modelled and constructed light curves, serving as an additional robust validation of our method and results (see crosses in Fig. 20). Using the ^{56}Ni abundance derived from our synthetic spectra ($0.76 M_\odot$), we compute the peak luminosity using a version of Arnett rule as described in Stritzinger & Leibundgut (2005), using our rise time of 18.74 d. We find a peak luminosity of $L_{\text{peak}} = 1.51 \pm 0.1 \times 10^{43}$ ergs s^{-1} . This result aligns with the peak luminosity value derived from our synthetic spectra yields, if we take in account the uncertainties associated with distance, photometry, and the method of integration. It is worth noting that this approximation, while providing a reasonable estimate, does not take into account the distribution of ^{56}Ni throughout the ejecta. To account for this distribution, we conduct a detailed modelling of the light curve in the subsequent subsection, offering a more accurate assessment.

8.1 Modelling the bolometric light curve

One independent way to test the results of abundance tomography is to use the density and abundance distributions derived from spectral modelling to compute a synthetic light curve. This should in principle reproduce the observed one, if the tomography results are reasonably correct, as the light curve depends on the mass and distribution of ^{56}Ni and on the opacity in the ejecta, which depends on the composition of the ejecta and governs the outward diffusion of the photons.

Starting from the tomography results, we used our Monte Carlo SN light curve code to compute a synthetic bolometric light curve to be compared to the one obtained from the observations. The code is based on the principles set out in Cappellaro et al. (1997) and Mazzali et al. (2001a). The basic assumption is that opacity in a SN Ia is dominated by line opacity (Pauldrach et al. 1996), and therefore it depends on composition: heavier elements such as iron have more electrons and therefore a complex energy level structure and more spectral lines that can in principle hinder photon diffusion than do lighter elements such as silicon. In our calculations, opacity is treated using a scheme outlined in Mazzali & Podsiadlowski (2006), which includes the dependence of the opacity on the number of effective lines and temperature through the Fe mass fraction and time after the explosion, respectively.

The deposition of the energy carried by the γ -rays and positrons is computed exactly like in the nebular code, but then the energy that has gone into heating the gas is transformed into ‘optical packets’ which diffuse in the ejecta, encountering an opacity determined locally by the composition in the various ejecta layers. When a packet escapes, it is accounted as contributing to the emerging luminosity at that particular time. The code is grey in frequency, and so the output is a bolometric luminosity. This compares to the bolometric luminosity obtained from the data, but it includes radiation at all wavelengths, and so it is a ‘true’ bolometric luminosity.

The synthetic light curve for iPTF16abc is shown in Fig. 20. It matches the observed one quite well in the rising part, which is an indication of the correct estimate of the outer distribution of ^{56}Ni , and near peak, which supports the mass estimate. It does a good job also in the early declining phase, while it departs from the observed light curve at later times, but clearly not at the nebular epoch, which is not shown in Fig. 20. These differences may be attributed to the progressive shifting of the flux towards the infrared, whose contribution is difficult to estimate because this wavelength range is not covered by the data of iPTF16abc. It is now known that the IR becomes a strong component at late times (Deckers et al. 2023). Still, our result confirms that the estimate of the ^{56}Ni mass ejected is correct, and the fact that the width of the light curve near maximum is correctly reproduced is also supportive of our estimate of M_{ej} and E_k , i.e. of our choice of explosion model.

9 DISCUSSION

iPTF16abc demonstrates weaker Fe III lines in its early spectra compared to both SNe 1999aa and 1991T. This difference is evident in Fig. 21, where we measure the pseudo equivalent width (PEW) of the Fe III trough around 4800 Å following the method described in Hachinger et al. (2006). This trend is further confirmed when we examine the abundance levels (cf. Fig. 22). Notably, iPTF16abc exhibits approximately 7–10 times less iron than both SNe 1999aa and 1991T at velocities larger than 15 000 km s^{-1} . However, this disparity diminishes at deeper layers, where iPTF16abc’s iron abundance aligns more closely with that of other events. This is supported by PEW measurements of iron emission lines in the nebular phase

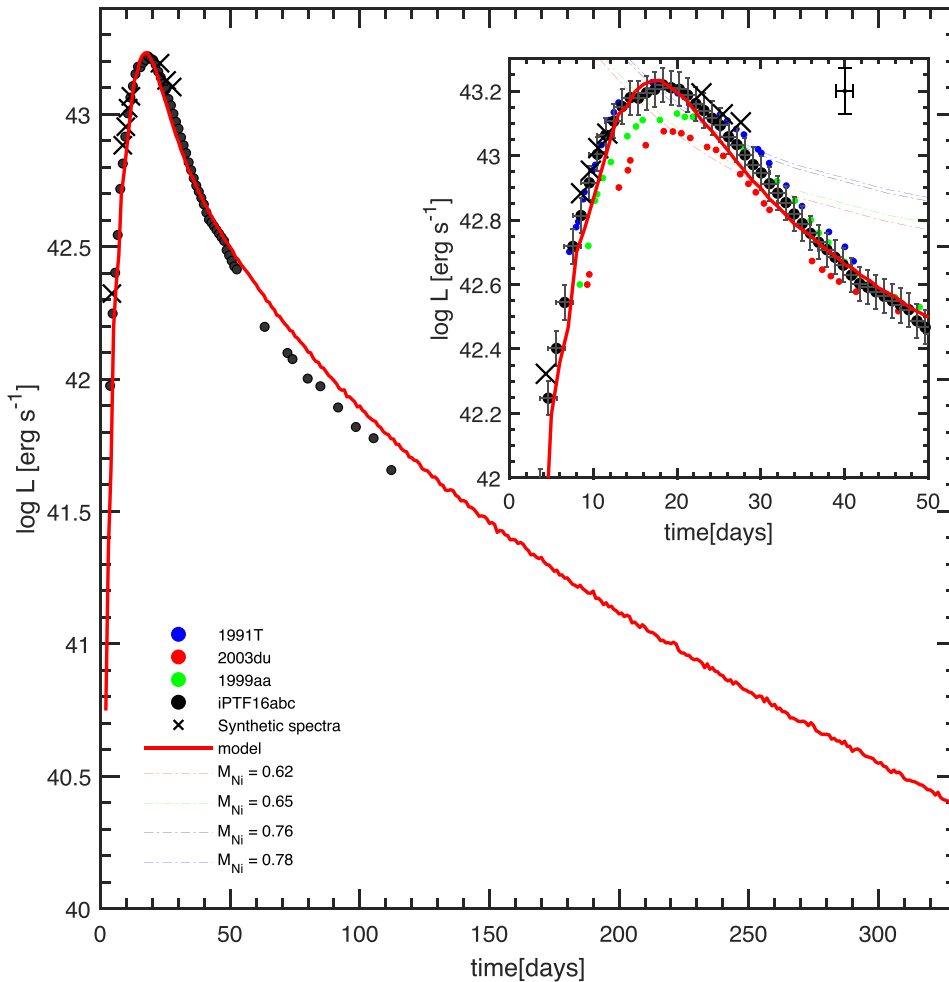


Figure 20. The modelled bolometric light curve (red line) of iPTF16abc is plotted alongside the bolometric light curves of SNe 1991T, 1999aa, and 2003du. Days are with respect to the assumed explosion time. Black dots are bolometric luminosities calculated using the photometry data of Miller et al. (2018). Crosses represent bolometric luminosities calculated using our synthetic spectra. Curves in dashed lines in the subplot represent unique instantaneous energy release rates resulting from the decay of ^{56}Ni , computed for different ^{56}Ni masses for each supernova as suggested from the modelling (see Tanaka et al. 2011; Sasdelli et al. 2014; Aouad et al. 2022). The plotted data points include errors originating from photometry, while the error bars inserted into the plot account for distance uncertainties, considering a distance modulus error of 0.15 mag, as outlined in Makarov et al. (2014).

(see Miller et al. (2018)). Consequently, this suggests that the relative weakness of Fe III lines during the photospheric phase is likely due to variations in abundance within the outermost shells rather than being driven by ionization-related luminosity effects.

This observation is particularly significant, highlighting that objects with weaker early Fe III lines may have comparable or even higher luminosities than those with stronger lines like SNe 1999aa and 1991T. This comparison becomes particularly intriguing when examining the 2003fg-like events. Despite their elevated luminosities, this subclass is recognized by weak Fe III lines (Ashall et al. 2021). Moreover, the outermost shells' supersolar abundance of stable iron in iPTF16abc, coupled with the existence of ^{56}Ni , is a topic of interest. While the presence of ^{56}Ni is undeniably linked to explosive nucleosynthesis, we should also remain receptive to the possibility that the presence of stable iron might be connected to the progenitor star's original metallicity. This alternative explanation should not be dismissed, especially in cases where the abundance is supersolar, as observed in SN 1999aa (Aouad et al. 2022), SN 1991T (Mazzali et al. 1995; Sasdelli et al. 2014), SN 2002bo (Stehle et al. 2005), SN 2010jn (Hachinger et al. 2013), and iPTF16abc. Such

instances may suggest that progenitors with above-solar metallicity do not necessarily lead to dimmer events, as suggested, for instance, in Timmes, Brown & Truran (2003). An alternative explanation may also be multidimensional effects involving bubbles of burned material rising to outer regions, or large-scale turbulent mixing giving rise to the presence of IGEs at the outer shells (Hachisu et al. 1992; Aspden, Bell & Woosley 2010).

When examining the spectral evolution from the spectroscopically normal to the peculiar luminous 91T-like events, the attenuation of the Si II λ 6355 line can be more attributed to abundance-related factors rather than influences of ionization (Sasdelli et al. 2014; Aouad et al. 2022). Interestingly, upon comparing the abundance profiles of different events (cf. Fig. 22), silicon displays a noticeable decline in the outermost shells across the three 91T-like objects we have modelled, within a comparable velocity range. A similar observation has been recently proposed by O'Brien et al. (2023), where they model the optical spectra of 40 SNe Ia encompassing both normal and 91T-like classifications. They deduce a deficiency in intermediate-mass elements (IMEs) abundance in the 91T-like events compared to those classified as normal (see also Mazzali et al.

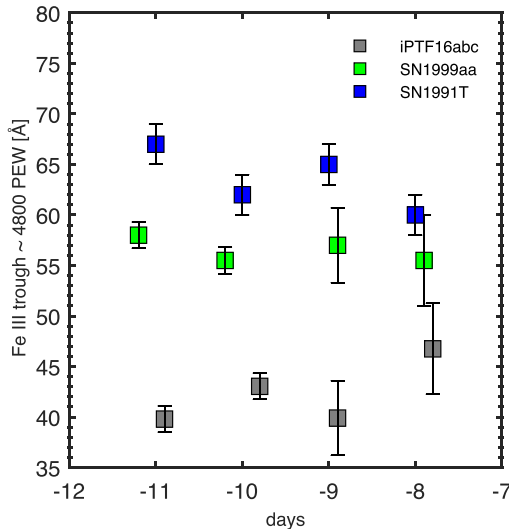


Figure 21. Comparison of the pseudo equivalent width of the Fe III trough, around 4800 Å, in the early spectra of iPTF16abc with those measured for SNe 1999aa and 1991T. The measurements were carried out following the approach described in Hachinger, Mazzali & Benetti (2006). Days are with reference to B maximum.

2007). This behaviour holds true for sulfur abundance as well. This trend implies the existence of a distinct burning regime within this specific subclass of supernovae, setting it apart from the dynamics that characterize spectroscopically normal events like SN 2003du. Within the operative regime among the 91T-like events, it appears that the burning front abruptly ceases within a velocity range spanning between 12 000 and 13 000 km s⁻¹. This cessation creates a division within the outer ejecta, resulting in two distinct regions characterized by differing degrees of burning activity, one marked by vigorous burning and the other characterized by subdued burning.

The persistent carbon features until two weeks post maximum display no resemblance to any SN Ia within the same spectroscopic subclass, namely SNe 1999aa and 1991T. Moreover, despite sporadic appearances of these attributes in the early spectra of events classified as normal, they are notably absent during the phase of maximum brightness and subsequent periods, e.g. SN2013du (Zheng et al. 2013), SN 2011fe (Nugent et al. 2011) (see also Parrent et al. 2011; Folatelli et al. 2012). Remarkably, these characteristics have consistently emerged in 2003fg-like events (Ashall et al. 2021), such as SN 2009dc (Taubenberger et al. 2011; Hachinger et al. 2012), SN 2006gz (Hicken et al. 2007), SN 2012dn (Chakradhari et al. 2014), and recently SN 2022pul (Siebert et al. 2023). This pattern is evident from early spectra up to two weeks after reaching peak intensity.

In Fig. 23, we plot the PEW of the C II λ 6580 and its velocity compared to a set of 2003fg-like SNe taken from Ashall et al. (2021). While the velocity of the line follows a similar trend to that observed in 2003fg-like events, the PEW displays a different pattern. It initially exhibits considerable strength at an early stage, experiences subsequent weakening, but unexpectedly strengthens again one week after maximum. This behaviour distinguishes it from other 03fg-like supernovae and reinforces the insights derived from our abundance analysis, which reveals an increase in carbon abundance in deeper layers, giving rise to a ‘bump’ around 10 000 km s⁻¹. Given this observation, it is plausible to speculate that this phenomenon arises from mixing driven by flame propagation asymmetries or clumps of unburned material along the line of sight (Parrent et al. 2011;

Folatelli et al. 2012). Alternatively, it may arise from a C-rich envelope, leading to the decrease of photospheric velocities as the ejecta interacts with this extended envelope. This interaction could give rise to the prominence of carbon lines and longer diffusion times, a scenario suggested for the 2003fg-like events (Ashall et al. 2021). This scenario may be considered viable for iPTF16abc given the low velocity of the Si II 6355 Å line (Miller et al. 2018, see). Finally, carbon could be the surviving material from a pulsation driven detonation (PDD; Ivanova, Imshennik & Chechetkin 1974; Khokhlov 1991a; Dessart et al. 2014). This is a scenario in which a failed deflagration expands the WD, creating a low density loosely bound envelope, such that, when the detonation occurs, an outer unburnt shell is left and the IME shell is confined in a narrow velocity range.

Regardless of the scenario, the identification of carbon in iPTF16abc is captivating, positioning this event as a link connecting the 03fg-like and 91T-like classifications. None the less, in addition to these spectroscopic parallels with 03fg-like events, iPTF16abc distinctively retains all the spectroscopic characteristics reminiscent of a 91T-like SNe Ia. This resemblance to the 91T-like SNe Ia persists into the nebular phase. Furthermore, when assessing the photometric attributes, iPTF16abc bears no resemblance to 03fg-like events, which are characterized by IR light curves devoid of a secondary maximum (Ashall et al. 2021). Additionally, the time of the i -band maximum occurs after to the B -band maximum in the events classified as 03fg-like. In iPTF16abc, it occurs three days before the B -band maximum, similar to the majority of 91T-like events (see Ashall et al. 2020).

The subdued intensity of the Ca II H&K feature in the early-phase spectra of iPTF16abc, compared to SN 1999aa, can easily be attributed to the distinct luminosities of the two objects. However, drawing definitive conclusions becomes challenging when juxtaposed with SN 1991T, particularly given the comparable bolometric light curves exhibited by these events, even when considering inherent uncertainties. The observed dissimilarities in the behaviour of the Ca II H&K lines do not offer sufficient grounds to categorize iPTF16abc as an intermediate object between SN 1999aa and SN 1991T. Based on the available data, it is more plausible to consider iPTF16abc as a similar object to SN 1991T, except for the Carbon features. The differences in the suppression of the Ca II H&K line could potentially be influenced by density variations in the outer layers affecting calcium recombination, or it could arise from different ionization levels due to varying temperatures.

It remains an open question whether SNe displaying intermediate properties between the ones observed in iPTF16abc and the ones observed in both SNe 1999aa and 1991T will be discovered, particularly concerning the strengths and temporal evolution of the Fe III, Ca II, H&K, C II, and Si II features. This could provide further insights into our understanding of the complex spectroscopic diversity observed in 91T-like SNe Ia.

10 CONCLUSIONS

We have modelled a time series of optical spectra to derive the abundance of the peculiar carbon rich, 91T-like type Ia supernova, iPTF16abc, and compare it to both SNe, 1999aa, and 1991T from one side, and the normal SN 2003du from the other side. Our main conclusions can be summarized as follows:

- (i) Delayed detonation density profiles align very well with iPTF16abc’s spectroscopic features, even though requiring minor adjustments in the outer shells.

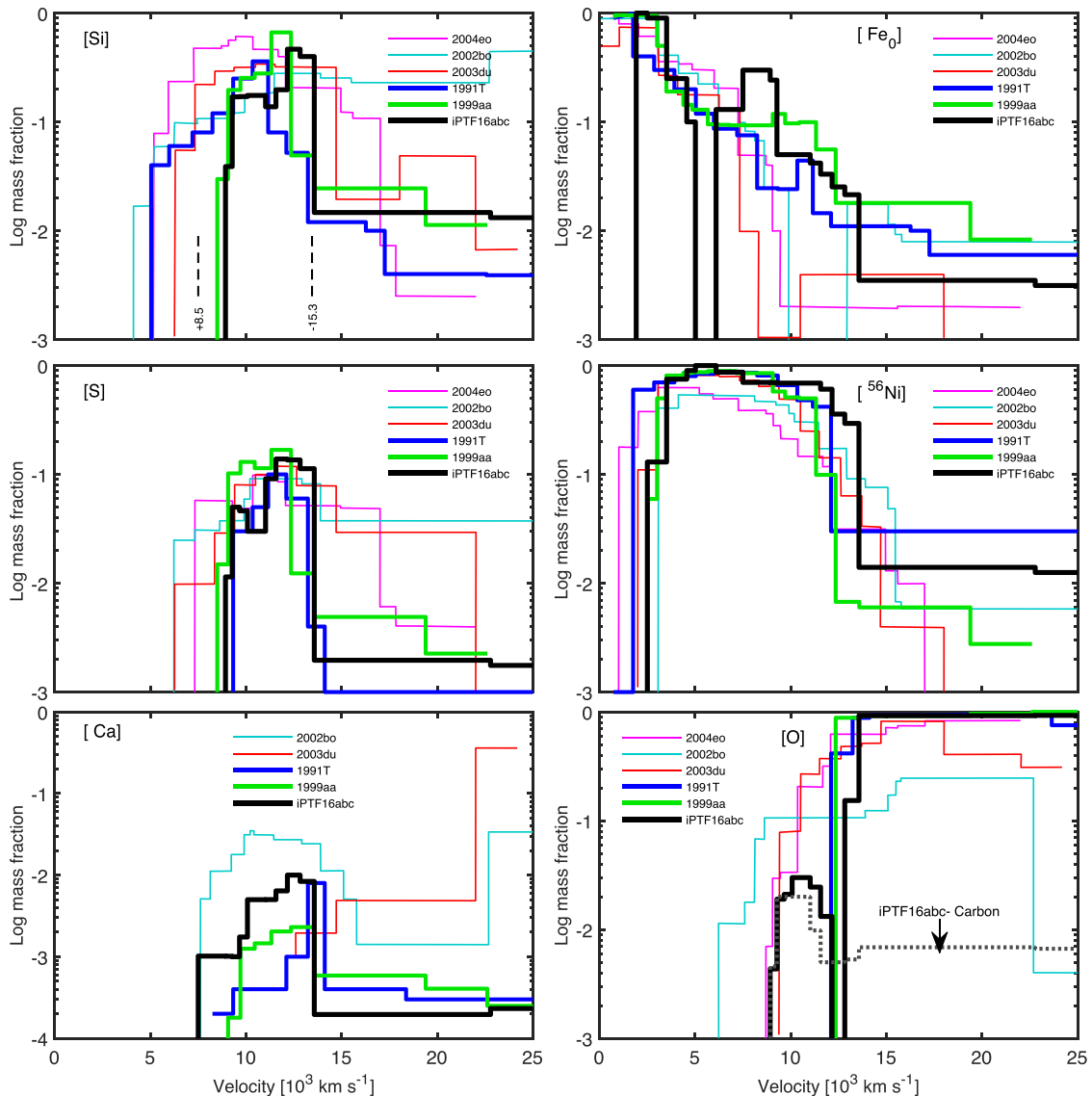


Figure 22. The distribution of the most important elements in SNe Iptf16abc, 1991T, 1999aa, and some spectroscopically normal SNe Ia. Left-hand side, top to bottom: Si, S, and Ca. Right-hand side, top to bottom: stable Fe, ⁵⁶Ni, O, and C. Iptf16abc exhibits very similar stratification properties to SNe 1999aa and 1991T, which are different than the spectroscopically normal events: the IMEs shell is narrow and is suddenly depleted above $\sim 12\,000\text{ km s}^{-1}$, oxygen dominates the outer shells and is sharply depleted below $\sim 12\,000\text{ km s}^{-1}$. Carbon extends deep and increases creating a noticeable peak around $10\,000\text{ km s}^{-1}$. The dashed lines in the first panel represent the velocities probed by our photospheric phase models, spanning from approximately days -15.3 to $+8.5$ relative to B maximum, while the regions below are probed by the nebular phase model.

(ii) The inner composition is dominated by stable IGEs ($0.20 M_{\odot}$) as in all SNe Ia followed by a ⁵⁶Ni dominated shell with a total mass of $0.76 M_{\odot}$ and a thin IME shell ($0.18 M_{\odot}$).

(iii) Iron abundance variations in the outermost layers explain the early weak Fe III lines, highlighting that 91T-like objects with weaker Fe III lines are not necessarily dimmer or cooler than those with stronger lines.

(iv) Detection of stable iron in the outermost shells, similar to SNe 1999aa and 1991T challenges existing explosion models. The idea that these are caused by bubbles of burned material rising to the outer layers is contradicted by the simultaneous presence of carbon within the ⁵⁶Ni dominated shell. This may suggest a potential link to the

progenitor’s original metallicity and may indicate that progenitors with above solar metallicity may not necessarily lead to dimmer events.

(v) Similar to SNe 1999aa and 1991T, the early Si II $\lambda 6355$ weakening results from silicon depletion in the outer shells. This distinct burning regime ends around $12\,000\text{ km s}^{-1}$, leaving incompletely burned outer layers and setting it apart from typical events.

(vi) Carbon co-exists with IGEs in the outermost shells, extending inward with a noticeable increase in deeper layers. This persistence of the carbon feature beyond the maximum light epoch establishes a unique connection with SN 2003fg-like events.

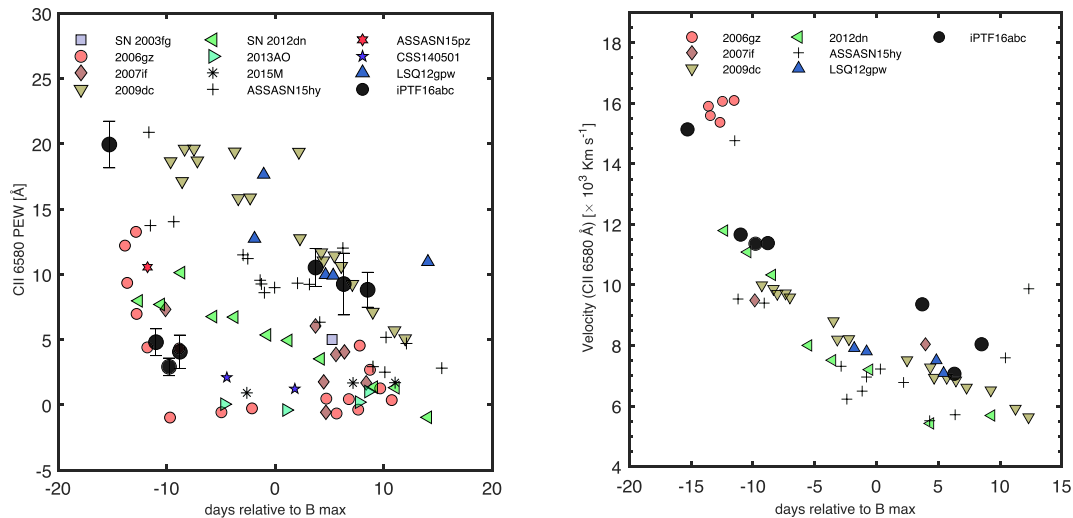


Figure 23. Left-hand panel: Pseudo equivalent width (PEW) of the C II 6580 Å observed in iPTF16abc, compared to a set of SNe 2003fg-like taken from Ashall et al. (2021). The line initially shows notable strength at an early stage but experiences a subsequent weakening before ultimately strengthening again, approximately one week after maximum light.

Right-hand panel: Velocity of the same line.

ACKNOWLEDGEMENTS

CA acknowledges support from NASA grants JWST-GO-02114, JWST-GO-02122, and JWST-GO-04522. Support for programs #2114, #2122, and #4522 were provided by NASA through a grant from the Space Telescope Science Institute, which is operated by the Association of Universities for Research in Astronomy, Inc., under NASA contract NAS 5–03127. The authors express their gratitude to Suhail Dhawan for sharing the spectra in readable format, and to Adam Miller for supplying the photometry data. Additionally, the authors extend their thanks to the anonymous referee for their meticulous review and valuable suggestions, which enhanced the overall quality of the paper.

DATA AVAILABILITY

The spectroscopic data underlying this article are available at the Weizmann Interactive Supernova Data Repository (WiSeREP; Yaron & Gal-Yam 2012).

REFERENCES

- Aouad C. J. et al., 2022, *MNRAS*, 515, 4445
 Arnett W. D., 1982, *ApJ*, 253, 785
 Ashall C., Mazzali P. A., 2020, *MNRAS*, 492, 5956
 Ashall C., Mazzali P. A., Pian E., James P. A., 2016, *MNRAS*, 463, 1891
 Ashall C. et al., 2018, *MNRAS*, 477, 153
 Ashall C. et al., 2020, *ApJ*, 895, L3
 Ashall C. et al., 2021, *ApJ*, 922, 205
 Aspden A. J., Bell J. B., Woosley S. E., 2010, *ApJ*, 710, 1654
 Asplund M., Grevesse N., Sauval A. J., Scott P., 2009, *ARA&A*, 47, 481
 Axelrod T. S., 1980, in Wheeler J. C., ed., *Texas Workshop on Type I Supernovae*. Springer, p. 80
 Benetti S. et al., 2005, *ApJ*, 623, 1011
 Bersten M. C., Mazzali P. A., 2017, in Alsabti A. W., Murdin P., eds, *Handbook of Supernovae*. p. 723
 Branch D. et al., 2006, *PASP*, 118, 560
 Cappellaro E., Mazzali P. A., Benetti S., Danziger I. J., Turatto M., della Valle M., Patat F., 1997, *A&A*, 328, 203
 Cardelli J. A., Clayton G. C., Mathis J. S., 1989, *ApJ*, 345, 245
 Castor J. I., 1970, *MNRAS*, 149, 111
 Chakradhari N. K., Sahu D. K., Srivastav S., Anupama G. C., 2014, *MNRAS*, 443, 1663
 Childress M. J., Filippenko A. V., Ganeshalingam M., Schmidt B. P., 2014, *MNRAS*, 437, 338
 Colgate S. A., McKee C., 1969, *ApJ*, 157, 623
 Contardo G., Leibundgut B., Vacca W. D., 2000, *A&A*, 359, 876
 Courtois H. M., Tully R. B., 2015, *MNRAS*, 447, 1531
 Deckers M. et al., 2023, *MNRAS*, 521, 4414
 DerKacy J. M. et al., 2024, *ApJ*, 961, 187
 Dessart L., Blondin S., Hillier D. J., Khokhlov A., 2014, *MNRAS*, 441, 532
 Dhawan S. et al., 2018, *MNRAS*, 480, 1445
 Dutta A., Singh A., Anupama G. C., Sahu D. K., Kumar B., 2021, *MNRAS*, 503, 896
 Ferretti R. et al., 2017, *A&A*, 606, A111
 Filippenko A. V., 1997, *ARA&A*, 35, 309
 Folatelli G. et al., 2012, *ApJ*, 745, 74
 Fukugita M., Shimasaku K., Ichikawa T., 1995, *PASP*, 107, 945
 Gal-Yam A., 2016, *TNS*, 2016-261, 1
 Ganeshalingam M. et al., 2012, *ApJ*, 751, 142
 Garavini G. et al., 2004, *AJ*, 128, 387
 Hachinger S., Mazzali P. A., Benetti S., 2006, *MNRAS*, 370, 299
 Hachinger S., Mazzali P. A., Taubenberger S., Pakmor R., Hillebrandt W., 2009, *MNRAS*, 399, 1238
 Hachinger S., Mazzali P. A., Taubenberger S., Fink M., Pakmor R., Hillebrandt W., Seitenzahl I. R., 2012, *MNRAS*, 427, 2057
 Hachinger S. et al., 2013, *MNRAS*, 429, 2228
 Hachisu I., Matsuda T., Nomoto K., Shigeyama T., 1992, *ApJ*, 390, 230
 Hicken M., Garnavich P. M., Prieto J. L., Blondin S., DePoy D. L., Kirshner R. P., Parrent J., 2007, *ApJ*, 669, L17
 Hillebrandt W., Niemeyer J. C., 2000, *ARA&A*, 38, 191
 Howell D. A. et al., 2006, *Nature*, 443, 308
 Iben I. J., Tutukov A. V., 1984, *ApJS*, 54, 335
 Ivanova L. N., Imshennik V. S., Chechetkin V. M., 1974, *Ap&SS*, 31, 497
 Iwamoto K., Brachwitz F., Nomoto K., Kishimoto N., Umeda H., Hix W. R., Thielemann F.-K., 1999, *ApJS*, 125, 439
 Karachentsev I. D., Kudrya Y. N., Karachentseva V. E., Mitronova S. N., 2006, *Astrophys.*, 49, 450
 Khokhlov A. M., 1991a, *A&A*, 245, L25
 Khokhlov A. M., 1991b, *A&A*, 245, 114

- Kushnir D., Katz B., Dong S., Livne E., Fernández R., 2013, *ApJ*, 778, L37
- Lentz E. J., Baron E., Hauschildt P. H., Branch D., 2002, *ApJ*, 580, 374
- Li W. et al., 2003, *PASP*, 115, 453
- Livio M., Mazzali P., 2018, *Phys. Rep.*, 736, 1
- Lucy L. B., 1999a, *A&A*, 344, 282
- Lucy L. B., 1999b, *A&A*, 345, 211
- Makarov D., Prugniel P., Terekhova N., Courtois H., Vauglin I., 2014, *A&A*, 570, A13
- Mazzali P. A., 2000, *A&A*, 363, 705
- Mazzali P. A., Lucy L. B., 1993, *A&A*, 279, 447
- Mazzali P. A., Podsiadlowski P., 2006, *MNRAS*, 369, L19
- Mazzali P. A., Danziger I. J., Turatto M., 1995, *A&A*, 297, 509
- Mazzali P. A., Chugai N., Turatto M., Lucy L. B., Danziger I. J., Cappellaro E., della Valle M., Benetti S., 1997, *MNRAS*, 284, 151
- Mazzali P. A., Nomoto K., Cappellaro E., Nakamura T., Umeda H., Iwamoto K., 2001a, *ApJ*, 547, 988
- Mazzali P. A., Nomoto K., Patat F., Maeda K., 2001b, *ApJ*, 559, 1047
- Mazzali P. A. et al., 2005, *ApJ*, 623, L37
- Mazzali P. A., Röpke F. K., Benetti S., Hillebrandt W., 2007, *Science*, 315, 825
- Mazzali P. A., Sauer D. N., Pastorello A., Benetti S., Hillebrandt W., 2008, *MNRAS*, 386, 1897
- Mazzali P. A. et al., 2014, *MNRAS*, 439, 1959
- Mazzali P. A. et al., 2015, *MNRAS*, 450, 2631
- Miller A. A. et al., 2018, *ApJ*, 852, 100
- Nomoto K., Thielemann F. K., Yokoi K., 1984, *ApJ*, 286, 644
- Nugent P., Phillips M., Baron E., Branch D., Hauschildt P., 1995, *ApJ*, 455, L147
- Nugent P. E. et al., 2011, *Nature*, 480, 344
- O'Brien J. T. et al., 2023, preprint ([arXiv:2306.08137](https://arxiv.org/abs/2306.08137))
- Pankey Titus J., 1962, PhD thesis, Howard University, Washington DC
- Parrent J. T. et al., 2011, *ApJ*, 732, 30
- Parrent J., Friesen B., Parthasarathy M., 2014, *Ap&SS*, 351, 1
- Pauldrach A. W. A., Duschinger M., Mazzali P. A., Puls J., Lennon M., Miller D. L., 1996, *A&A*, 312, 525
- Perlmutter S. et al., 1998, *Nature*, 391, 51
- Phillips M. M., 1993, *ApJ*, 413, L105
- Riess A. G. et al., 1998, *AJ*, 116, 1009
- Sasdelli M., Mazzali P. A., Pian E., Nomoto K., Hachinger S., Cappellaro E., Benetti S., 2014, *MNRAS*, 445, 711
- Scalzo R. et al., 2012, *ApJ*, 757, 12
- Schlafly E. F., Finkbeiner D. P., 2011, *ApJ*, 737, 103
- Siebert M. R. et al., 2023, *ApJ*, 960, 88
- Sobolev V. V., 1960, *Moving Envelopes of Stars*. Harvard University Press, Cambridge
- Stehle M., Mazzali P. A., Benetti S., Hillebrandt W., 2005, *MNRAS*, 360, 1231
- Stritzinger M., Leibundgut B., 2005, *A&A*, 431, 423
- Tanaka M. et al., 2008, *ApJ*, 677, 448
- Tanaka M., Mazzali P. A., Stanishev V., Maurer I., Kerzendorf W. E., Nomoto K., 2011, *MNRAS*, 410, 1725
- Taubenberger S. et al., 2011, *MNRAS*, 412, 2735
- Theureau G., Hanski M. O., Coudreau N., Hallet N., Martin J. M., 2007, *A&A*, 465, 71
- Timmes F. X., Brown E. F., Truran J. W., 2003, *ApJ*, 590, L83
- Wang X. et al., 2009, *ApJ*, 699, L139
- Whelan J., Iben Icko J., 1973, *ApJ*, 186, 1007
- Willick J. A., Courteau S., Faber S. M., Burstein D., Dekel A., Strauss M. A., 1997, *ApJS*, 109, 333
- Woosley S. E., Kasen D., Blinnikov S., Sorokina E., 2007, *ApJ*, 662, 487
- Yaron O., Gal-Yam A., 2012, *PASP*, 124, 668
- Zheng W. et al., 2013, *ApJ*, 778, L15

This paper has been typeset from a $\text{\TeX}/\text{\LaTeX}$ file prepared by the author.